NATIONAL OPTICAL ASTRONOMY OBSERVATORIES

Preprint Series

NOAO Preprint No. 860

SOLAR-CYCLE CHANGES IN GONG P-MODE WIDTHS AND AMPLITUDES 1995-98

R. W. Komm

R. Howe

and

F. Hill

(National Solar Observatory, National Optical Astronomy Observatories)

Accepted By: Astrophysical Journal

November 1999

Operated for the National Science Foundation by the Association of Universities for Research in Astronomy, Inc.

SOLAR-CYCLE CHANGES IN GONG P-MODE WIDTHS AND AMPLITUDES 1995–98

R.W. Komm, R. Howe, F. Hill

National Solar Observatory, National Optical Astronomy Observatories[1]*,*
950 N. Cherry Ave., Tucson, AZ 85726

ABSTRACT

We search for a solar cycle variation in mode widths and amplitudes derived from 3-month GONG time series. The variation of mode width and amplitude observed in GONG data are the combined effects of fill factor, temporal variation, and measurement uncertainties. The largest variation is caused by the fill factor resulting in modes with increased width and reduced amplitude when fill is lower. We assume that the solar cycle variation is the only other systematic variation beside the temporal window function effect. We correct all currently available data sets for the fill factor and simultaneously derive the solar cycle variation. We find an increase of about 3% on average in mode width from the previous minimum to Oct. 1998 and a decrease of about 7% and 6% in mode amplitude and mode area (width × amplitude). We find no l dependence of the solar-cycle changes. As a function of frequency, these changes show a maximum between 2.7 and 3.3 mHz with about 47% higher than average values for mode width and about 29% and 36% higher ones for mode amplitude and area. We estimate the significance of these rather small changes by a pre-whitening method and find that the results are significant at or above the 99.9% level with mode area showing the highest level of significance and mode width the lowest. The variation in background amplitude is most likely not significant and is consistent with a zero change.

Subject headings: Sun: activity — Sun: evolution — Sun: oscillations

1. INTRODUCTION

We study mode widths, amplitudes, and area (width × amplitude) derived from 108-day GONG time series and search for variations of these mode parameters with the solar cycle. These quantities provide information about p-mode excitation and damping. The source of the p-modes is thought to be due to stochastic excitation by the release of acoustic energy from sources near the

[1]Operated by the Association of Universities for Research in Astronomy, Inc. under cooperative agreement with the National Science Foundation.

top of the turbulent convection zone (cf., for example, Rast 1999; Rimmele et al. 1995; Goldreich, Murray, & Kumar 1994; Balmforth 1992; Osaki 1990, and references therein). The mode width is inversely proportional to the lifetime and thus contains information about the damping of modes, the mode amplitude is related to the mode energy, and the mode area reflects the acoustic power of the mode.

Solar-cycle changes in central mode frequencies and related splitting a-coefficients are now well-established (Howe, Komm, & Hill 1999, and references therein). However, solar-cycle changes of mode widths and amplitudes are less well studied due to the large number of observational effects on this measurement. Jefferies et al. (1990, 1991) and Meunier (1997) measured the solar cycle dependence of mode width using South Pole Ca K intensity data. Jefferies et al. (1990) found that the widths for modes with l values between $l = 80$ to 100 and $\nu \approx 3$ mHz are larger during 1981 (high activity) than in 1987 (low activity). Jefferies et al. (1991) state that this is consistent with an increase in mode width with increasing activity. They also predict that mode power decreases with increasing activity on the basis that the p-mode power is inversely proportional to the mode width (Osaki 1990) and assuming that the acoustic power pumped into the p-modes is constant with the solar cycle. Meunier (1997) found that the widths of intermediate-degree modes were on average smaller in 1998 (high activity) than in 1994 (low activity) which is the opposite of the previous South Pole results. Pallé, Régulo, & Roca Cortés (1990a,b) and Elsworth et al. (1993) used integrated sunlight velocity data to measure modes with $l = 0$ to 2. Pallé, Régulo, & Roca Cortés (1990a) found an inverse relation between mode power (area under the peaks) and solar activity using Observatorio del Teide measurements from 1977 to 1989 with a variation in power of about 40% depending on l value studied. In Pallé, Régulo, & Roca Cortés (1990b), they also report an increase in line width with increasing activity for $l = 0$. Elsworth et al. (1993) used observations obtained with the Birmingham Solar Oscillations Network ('BISON') during 1981 to 1992. They found that mode power decreases with increasing activity with a variation of about 35% between maximum and minimum constant for all l values. However, they found no significant variation of mode width with the solar cycle.

The variation of mode width and amplitude in GONG data is the combined effect of fill factor, temporal variation, and measurement uncertainties. The largest variation is caused by the gaps in the temporal window function; the fill factor is between 80% and 90% for GONG data. Being equivalent to a convolution with a broadened window in the Fourier domain, these gaps lead to modes with increased width and reduced amplitude. We assume that the solar cycle variation is the only other systematic variation beside the temporal window function effect and that the measurement uncertainties are essentially random fluctuations. We fit all currently available data sets simultaneously for the temporal window correction (fill factor) and for the solar cycle variation. We then estimate the significance of theses changes using a prewhitening technique. We find small but significant changes in mode width, amplitude, and area with the solar cycle and discuss the results.

2. DATA AND ANALYSIS

2.1. Data Sets

The data were processed through the GONG pipeline (Hill et al. 1996), producing power spectra of three GONG months' duration for each l and $|m|$ up to $l = 150$. The 3-month (with 1 GONG month being 36 days) time span was chosen to give adequate resolution of the modes while allowing the study of temporal variations. The 33 time periods analyzed, their temporal fill factors, and the corresponding average values of two measures of solar magnetic activity, are summarized in Table 1. The temporal fill for a 3-month period ranges from 0.77 to 0.92, with an unfortunate slight tendency towards lower fill in the more recent, higher-activity sets which may be associated with the adverse weather conditions due to the 1997-8 El Niño phenomenon. It should be noted that not all the periods used in this study are independent.

The mode parameters for each n, l, m mode were estimated from the 3-month power spectra using the standard GONG analysis (Anderson, Duvall, Jr., & Jefferies 1990), which fits modes up to $l = 150$. The peak-fitting algorithm has two types of error flags related to the quality of the fit to a mode. One is based on heuristic assumptions about the modes; the other indicates numerical difficulties (Hill et al. 1998). The heuristic flag includes, for example, a test to ensure that the fit has not locked onto the first guess; that the fitted width is within a factor of two of the first guess width; etc. The numerical flag indicates how well the minimization of the likelihood function converges and distinguishes between failure to converge, convergence with some difficulty, and strict convergence. Strict convergence is necessary but not sufficient for a good fit. Mode parameters from fits that did not pass all the heuristic tests and meet the strict convergence condition were excluded from this analysis.

The peak-fitting algorithm fits symmetric Lorentzian profiles to the asymmetric mode peaks in the power spectra. This will introduce a systematic error in the absolute values of the measured mode parameters which varies for different l and n and is different between velocity and intensity. At present, it is not well-known to what extent the mode asymmetry changes with the solar cycle. Meunier (1997) reported a change in asymmetry for intensity measurements, but given the differences between velocity and intensity her result cannot easily be extrapolated to velocity measurements. Thus, while we cannot completely rule out the possibility that some of the solar-cycle variations measured by us are affected by changes in asymmetry, we expect that the net effect is small since we average over many l and n values and since a strongly asymmetric peak most likely triggers one of the error flags of the peak-fitting algorithm.

We have studied mode width, amplitude, area (width × amplitude), and background amplitude as a function of two activity measures: sunspot number and magnetic flux. The sunspot number values were taken from the National Solar Observatory (Sacramento Peak) archive[2] and

[2]available at ftp://ftp.sunspot.noao.edu/pub/sunspots/spots.list

the magnetic flux (in Gauss) from the Kitt Peak synoptic charts[3]. We averaged the Kitt Peak synoptic maps over the 180 positions equidistant in sine latitude and over 4×360 positions in time representing 108 days. The relations between various activity measures, and in particular the temporal phase differences, have been discussed in some detail by Bachmann & White (1994). Figure 1 shows the average magnetic flux (in Gauss) and the sunspot numbers during the relevant time period. The two activity measures show a large linear correlation of 0.99, while they differ in some details. We therefore expect them to lead to essentially the same results and their comparison serves mainly as a consistency check.

2.2. Temporal Window Correction

GONG time series have gaps in the temporal window function with a typical fill of 80% to 90%; gaps in the temporal window are equivalent to a convolution with a broadened window in the Fourier domain. This leads to peaks with increased width and reduced amplitude with respect to uninterrupted observations, while the frequencies are not affected. For a variety of reasons, such as computation time and accuracy, we do not perform any temporal deconvolution of the spectrum prior to the peakfinding. Instead, we empirically determine a correction factor for both the widths and amplitudes, as described in more detail in Komm et al. (1999). The gaps in the GONG data are very short compared to the length of the time series and they show diurnal sidelobes, which are small compared to single-station data but are noticeable and dominate the gap structure. Due to this qualitative similarity, we assume that the effect depends only on the fill factor and not on the details of the gap structure of the temporal window.

To represent each (l, n) multiplet, we calculate weighted average values of the parameters. We include only multiplets where at least one third of all $(2l + 1)$ values are present. At $l \leq 10$, the averages are less well-defined due to the relatively small number of modes in a multiplet. For each multiplet, mode width and amplitude show a (m/l) dependence due to the spatial mask used in the reduction of GONG data. Amplitudes show a V-shaped dependence that is taken into account by a polynomial of $(m/l)^{2k}$ with $k = 0$, 1, and 2. The mode area, width $\times$ amplitude, and the background amplitude show a similar V-shaped (m/l) dependence. For mode amplitude and related parameters, we use the fitted values at $(m/l) = 0.0$ and at $(m/l) = 1.0$ as the values representative of each multiplet.

The mode width shows a Λ-shaped (m/l) dependence that is less pronounced than the amplitude variation and is mainly noticable at high and low n values. The number of multiplets at high n is small due to the mode resolution criterion, while the number of multiplets at low n is reduced by the one-third-present criterion. Thus, for the mode width, it is sufficient to calculate a weighted mean. Figure 2 shows an example of the four parameters as a function of (m/l) for a

[3]available at http://www.nso.noao.edu/nsokp/dataarch.html

given multiplet. From this figure, it is obvious that the standard deviation of the mean is about 10% of the mean value which stresses the importance of large data sets in order to derive significant results.

For each l, the widths vary strongly with the fill factor at intermediate n values, while they vary slightly or are almost constant at low and high n values, as in the example in Figure 3. Figure 3 also shows that a linear fit describes the variation very well. Using the linear fit, the widths extrapolated close to a 100% fill factor agree reasonably well (within 10%) with SOI/MDI data, analyzed with the GONG peakfinding algorithm, and with the deconvolved GONG data, as discussed in Komm et al. (1999). The SOI/MDI time series have very different window functions compared to GONG time series. But, since they have fill factors close to 100%, the mode parameters derived from them should be close to the 'true' values regardless of the details of the window function.

We then represent the variation of the width of each (l, n) multiplet by a polynomial in fill factor. To determine the degree necessary to adequately represent the data, we divide the 33 time samples into two subsets, fit one subset with the polynomial and calculate the average in-sample error (average error of the fitted subset) and the average out-of-sample error (average error of the fit with regard to the excluded subset). We repeat this procedure for various degrees of the fitting polynomial. The in-sample error is expected to decrease with increasing model complexity (if the model is adequate), while the out-of-sample error will decrease up to a certain degree and then increase again when the model overfits the data. The minimum in the out-of-sample error as a function of degree defines the best model. This method of cross-validation is described and discussed, for example, in Gershenfeld (1999) and Goutte (1997).

The top panel of Figure 4 shows the results for dividing the data sets at random into two subsets of 17 and 16 time samples. The values are weighted least-squares errors normalized by the in-sample error of the linear fit. The in-sample error ($\times$) decreases as expected with increasing degree of the fitting polynomial. The out-of-sample error ($\square$) decreases with increasing degree, shows a minimum at the quadratic fit and increases for higher-order polynomials, indicating that a quadratic fit is the best model. The bottom panel of Figure 4 shows the results for excluding the four time samples with highest fill factor. Again the in-sample error decreases with increasing degree. The minimum of the out-of-sample error occurs for a linear fit, indicating that it is the best model. Since the goal of the fill factor correction is to be able to extrapolate to a 100% fill, the second test is more relevant than the first. We repeated these two tests including the three SOI/MDI time samples analyzed with the GONG peakfinding algorithm and found that in this case the linear fit is the best model for random division and for exclusion of values with high fill factor. From this simple cross-validation, we conclude that the relation between width, amplitude, etc. and fill factor is to first order a linear relation and that higher-order corections have to be studied more carefully before including them.

Therefore, we apply a linear regression to correct the mode parameters of a given (l, n) multiplet

for the temporal window function.

$$\Gamma(fill) = intercept + slope * (1 - fill) \quad (1)$$

We perform a linear fit in fill factor for all (l, n) multiplets that are good fits according to the peakfind error flags that are resolved according to $d\nu/dl > 2\Gamma$ and where at least one third of the $(2l + 1)$ modes are present.

The resulting slopes normalized by the intercepts (fill of 100%) as a function of l and ν show that the effect of the temporal window function is strongest near $l \approx 40$ and $\nu \approx 3.0$ mHz (Figure 5). For example, a slope of 600% means that the width measured at 80% fill is 120% larger than the corresponding width at 100% fill. The intercepts (fill of 100%) of the linear fits are extrapolated estimates of the 'true' mode parameters as they would be determined from GONG observations without gaps (Figure 6), which we will investigate in a separate study.

2.3. Solar Cycle Variation

To search for a solar cycle variation, we fit all currently available data sets simultaneously for the temporal window correction (fill factor) and for the solar cycle variation, by adding a polynomial fit as a function of magnetic activity to the linear regression term in fill factor. Figure 7 shows an example of the variation of the four mode parameters studied here as a function of magnetic activity for a single multiplet. In this particular example, mode width and amplitude show a clear variation with activity, but it is about one order of magnitude smaller than the corresponding variation due to the fill factor. The linear correlation is only about 0.6 between these two parameters and the two activity indices, while it is about 0.9 between any of the four mode parameters and fill factor. Mode area and background amplitude show no significant variation with activity level in this example with a correlation coefficient of about 0.2 and 0.3 respectively.

We performed a cross-validation similar to the one in the previous subsection in order to determine the best model for the solar cycle variation. Figure 8 shows the results of randomly dividing the data set into two subsets and varying the degree of the polynomial in magnetic activity. The in-sample error decreases with increasing degree, while the out-of-sample error shows a minimum at the linear fit. We repeated this analysis for other random subdivisions and found the same result.

Therefore, we use a linear regression to describe the solar cycle variation in addition to a linear regression to describe the temporal window variation.

$$\Gamma(fill, B) = intercept + a_f * (1 - fill) + slope * (B - B_{min}) \quad (2)$$

We repeated this analysis for mode amplitude, mode area, and background amplitude and found that the solar cycle and the temporal window variation of these mode parameters is adequately described by a linear regression in each of the two variables as in Equation 2.

The correlation coefficients are a measure of fit quality with a large coefficient indicating that the model is appropriate. Figure 9 shows linear correlation coefficients of fill factor ($\times$) and magnetic activity ($\square$) for mode width. For $l \approx 25$ to $l \approx 120$, most activity correlations are about 99.9% significant and most fill factor correlations are well above the 99.9% level. The significance level decreases below 95% for higher and for lower l values. Mode amplitude and area show a similar behavior with mode area showing a less pronounced decrease at high and low l values. The mode background, on the other hand, shows the largest correlations for $l < 50$ and decreasing correlations with increasing l values. In the following section, we analyze only multiplets where both correlation coefficients of the regression analysis for fill factor and magnetic activity have a 95% or greater level of significance. This criterion safeguards against including multiplets where measurement uncertainties dominate. For example, mode area and background amplitude of $l = 50$, $n = 9$ (Figure 7) are excluded by this criterion. This reduces the number of multiplets from 1163 to about half this number for mode width, amplitude, and area. For the background amplitude, however, this threshold reduces the number of multiplets to about one fourth to one sixth which is too small to adequately cover the $(l\nu)$ diagram. We note that this threshold might exclude a few valid fits of multiplets at high or low n values where mode parameters are more or less independent of fill factor. The thresholding procedure is robust in the sense that the qualitative behavior and the average quantities presented in the following section do not depend on the applied threshold. Without thresholding, the scatter of the measurements is greater leading to larger standard deviations and the level of significance is overall smaller, but general trends and average quantities remain the same.

3. RESULTS

Figure 10 shows the results of the linear regression of mode width versus magnetic flux (Equation (2)). The top panel shows the slope normalized by the intercept as a function of l and the bottom panel shows the same as a function of ν, restricted to $l \geq 30$ to reduce scatter. The y-axis is in units of percent per Gauss. For example, with a difference between minimum and maximum activity in Figure 1 of about 6 G, a normalized slope of +0.5 reflects an increase in mode width of +3.0% compared to the width at solar minimum.

The normalized slope is 0.524 ± 0.025 averaged over all l and ν values; the mode width increases with increasing activity. The normalized slope is more or less independent of l. For $l < 30$, the slope seems to increase with decreasing l value. But, this is rather uncertain given the few data points. As a function of frequency, the normalized slopes show the largest values between 2.7 and 3.3 mHz with 0.769 ± 0.045 on average. Table 2 shows the average values and additional information. The difference between the minimum in Figure 1 and the previous solar maximum is about 14 G, which corresponds to an increase in width of about 7% on average and of 10% for modes with $2.7 < \nu < 3.3$ mHz.

Figure 11 shows the same as Figure 10 for mode amplitudes derived at $(m/l) = 1$. The

normalized slopes show a somewhat larger scatter than the slopes of the mode width, as reflected in the standard deviation values in Table 2. The means of the binned data are consistently located at negative values with -1.206 ± 0.037 on average; mode amplitudes decrease with increasing activity. For $l \geq 30$, there is almost no l dependence, while for smaller l the normalized slopes decrease with decreasing l value. This is the opposite behavior of the mode widths and demonstrates the inverse relation between mode width and amplitude. However, there is a quantitative difference leading to a non-zero slope of the product of the two, the mode area, as discussed below. The amplitude slopes show the same frequency dependence as the mode widths; the average departure from a zero slope is largest in the frequency range from 2.7 to 3.3 mHz.

Figure 12 shows the normalized slopes for the mode area, width × amplitude, derived at $(m/l) = 1$. The means of the binned data are consistently located at negative values with an average value of -0.971 ± 0.030, which implies that the effect is stronger in mode amplitude than in mode width. As expected from mode width and amplitude, the slopes show no l dependence for $l \geq 30$ and decrease with decreasing l for smaller l values. As for mode width and amplitude, the mode area slopes show the strongest departure from zero in the frequency range from 2.7 to 3.3 mHz with -1.317 ± 0.061 on average which is 36% larger than the average over all frequencies. The corresponding figures for mode area and amplitude derived at $(m/l) = 0$ show a similar behavior with smaller average slopes (see Table 2).

Figure 13 shows the normalized slopes for the background amplitude derived at $(m/l) = 1$ as a function of l. We include the plot of all multiplets (top panel), since in this case the 95% confidence threshold reduces the number of multiplets so much that showing them alone (bottom panel) might be misleading. In the top panel, there is no frequency dependence for $l < 80$, the values are more closely distributed around a zero slope than any of the other three mode parameters. For larger l values, there are two distinct distributions separated by mode frequency. For $\nu < 3$ mHz, the slopes show the same average values as for lower l values, while for $\nu \geq 3$ mHz, the slopes are systematically larger. The corresponding figure for the background amplitude derived at $(m/l) = 0$ shows a similar behavior.

The bottom panel shows that in this case the threshold leads to a selection of multiplets with mainly positive slopes in contrast to the mainly negative slopes in the top panel. For $(m/l) = 0$, the selection leads to mainly negative slopes close to the values without thresholding, but most of the multiplets with $l \geq 80$ and $\nu \geq 3$ mHz are excluded. For this reason, the average background amplitude slopes derived from $(m/l) = 0$ and $(m/l) = 1$ have different signs, as shown in Table 2. The variation in background amplitude is consistent with a zero change with a small trend toward negative values, except for $l > 80$ and $\nu \geq 3$ mHz, where the background amplitude increases with increasing activity.

In the region of $l > 80$ and $\nu \geq 3$ mHz, modes are broad enough to blend into ridges. Thus, an increase in mode width due to the solar cycle variation may cause the peakfind algorithm to overestimate the background in this region and consequently underestimate the mode amplitude.

Table 3 shows the same as Table 2 but excluding all values with $l > 80$ and $\nu > 3.0$ mHz. While mode width values are about 20% smaller in Table 3 compared to Table 2, mode amplitude and area values differ by about ±10%. Thus, the solar cycle variation of these parameters does not seem to be severely biased by potentially overestimated background amplitudes.

To test the significance of the increase in mode width with increasing activity and the corresponding decrease in amplitude and area, we randomize the order of the magnetic activity values in time (prewhitening) and perform the multiple linear regression in fill factor and randomized magnetic activity. We repeat this process 1,000 times making sure that we do not use the same randomization twice. Figure 14 shows the distributions of the average slopes of mode width (Γ), amplitude (A), area ($\Gamma \times A$), and background amplitude (b_0) for all $l \geq 30$ averaged over all frequencies. The measured average slope of the mode area is –5.1 standard deviations of the randomized distribution away from zero for $(m/l) = 1$ and –4.8 for $(m/l) = 0$ which is the largest departure from a zero slope. Mode amplitude slopes show a slightly smaller departure from zero with –4.9 and –3.7 and mode width slopes show the smallest departure of these three parameters with 2.8 standard deviations. Histograms limited to the frequency range of 2.8 to 3.2 mHz are very similar to the ones in Figure 14 leading to similar levels of significance. The background amplitude shows a value of 0.4 standard deviations for $(m/l) = 1$ and –1.6 for $(m/l) = 0$. Thus, the solar cycle related changes in mode width, amplitude, and area are significant at about the 99.9% level and higher, while the variation of the background amplitude is not significant and is consistent with a zero change.

As a consistency check, we correlate the measured magnetic activity (as a function of time) with the randomly distributed activity and plot this correlation versus the average slope of the randomized data sets. The top row of Figure 15 shows the resulting scatter plots for the mode area, which shows the highest level of significance. The correlation with magnetic activity shows a cloud of points centered around zero and elongated in the direction of the actual measurement (□) connected with a solid line. This elongation is present for the average over all frequencies and for the frequency range centered around 3 mHz. Thus, the average slope of the random sample gets increasingly closer to the measured average slope with increasing similarity between randomized activity and measured activity. Mode width and amplitude show a similar behavior with slightly more scatter, indicating that their variation with magnetic activity is indeed significant, while the backgound amplitude shows no preferred direction which is consistent with a zero change.

In addition, we calculated the correlation of the magnetic activity with the fill factor to see if the much larger correction for the temporal window could bias the regression in activity. The bottom row of Figure 15 shows a cloud of points without a preferred direction for mode area; mode width and amplitude show a similar behavior. After rebinning the correlations, the mean slope in each bin is close to zero. Thus, it is unlikely that their change with magnetic activity is simply an artifact of the temporal window correction. The background amplitude shows also a cloud of points without a preferred direction which is no surprise since its variation with activity is consistent with a zero change.

We repeat this analysis for sunspot numbers instead of magnetic flux and find essentially the same results. The l and frequency dependences of the resulting slopes are the same as shown in Figures 10 to 12. The average values in percent per sunspot number are listed in Table 4. For mode amplitude and area, the levels of significance are the same as for the magnetic flux, while for mode width the significance is slightly smaller. Figure 16 shows a comparison of normalized slopes derived from good fits common to the regression in magnetic flux and in sunspot numbers. The figure shows, as expected, a high linear correlation of 0.99 between the solar cycle variations of the four mode parameters derived from the two activity indices, which is as high as the correlation between sunspot numbers and magnetic flux. The background amplitude is the only one with fairly large scatter and also a non-zero intercept.

4. SUMMARY AND DISCUSSION

We find a strong correlation between mode width, amplitude, and area and the two activity indices used here, with sunspot numbers and magnetic flux leading to the same result. The level of significance of the solar cycle variation is highest for mode area and lowest for mode width. With a difference of about 14 G between the last solar minimum and the previous maximum, we would expect an increase of about 7% on average in mode width from minimum to maximum activity and a decrease of 16% and 13% in mode amplitude and area (width $\times$ amplitude). The background amplitude shows a small decrease which is not significant and its change is consistent with a zero change. An increase of about 7% in mode width over the solar cycle is about a factor of four smaller than the average shift in central mode frequency (≈ 0.4 μHz) assuming a median mode width of 1.5 μHz.

For stochastically excited modes, a broadening in mode width implies a reduced lifetime or increased damping of the modes during times of high magnetic activity. The reduction in mode area implies a reduction in the amount of acoustic energy pumped into the modes by turbulent convection. This agrees with the presumption that the presence of strong magnetic fields suppresses motions in a turbulent medium, which is known to occur for several solar surface phenomena. Previous analyses (Howe, Komm, & Hill 1999, 2000; Toomre et al. 2000) show that the solar cycle variation of flows observed in helioseismic data exists in about the upper 7 or 8% of the Sun or the upper quarter of the convection zone near the surface of the Sun. The frequency dependence of the solar cycle variation of p-mode frequencies indicates that the underlying structural changes occur near the solar surface (Libbrecht & Woodard 1990; Elsworth et al. 1994). This suggests that changes in width and area are due to changes of the physical conditions in the upper part of the mode cavity near the upper turning point.

A possible, specific mechanism by which magnetic activity can influence mode widths is the excitation of oscillations in flux tubes. Flux tubes are buffeted by p-modes which excite nonresonant oscillations in flux tubes (Bogdan et al. 1996; Hasan 1997; Hasan & Kalkofen 1998) leading to a balance between energy input from p-modes and losses through radiative damping and leakage

from flux tube boundaries. The excitation of resonant oscillations in flux tubes in unstratified atmospheres was studied, for example, by Ryutova & Priest (1993a,b). Resonant coupling with MHD waves (Pintèr & Goossens 1999) might also contribute to the damping of p-modes, as well as scattering of p-modes by flux tubes (Keppens, Bogdan, & Goossens 1994; Bogdan & Zweibel 1987). Thus, when the magnetic activity increases during the rising phase of the solar cycle, p-modes are increasingly damped by the interactions with the increasing number of flux tubes. Bogdan et al. (1996) modelled the absorption of p-modes by exciting longitudinal ('sausage') and transversal ('kink') modes in thin magnetic flux tubes and explicitely studied the contribution of this process to the width of p-modes. By comparing their theoretical results with p-mode widths measured by Korzennik (1990), they concluded that the contribution to the p-mode line width of p-mode absorption by flux tubes is of the order of a few to about 10%. This agrees within a factor of two with the solar-cycle variation of p-mode widths expected from our results.

It is known that strong downward plumes in intergranular lanes are a source of acoustic energy exciting p-modes (Rast 1999; Rimmele et al. 1995), that in plages vertical motions in the photosphere are suppressed in the presence of magnetic flux tubes (Title et al. 1992) and that rms velocities are reduced in regions of enhanced magnetic field in intergranular lanes (Nesis et al. 1996). Thus, the presence of flux tubes might suppress the downward plumes responsible for exciting p-modes. This suggestion is consistent with the observation by Gooode & Strous (1996) that in regions of the quiet Sun the local magnetic field appears to diminish both the average acoustic flux and the p-mode power. To see if such a filling factor argument might explain the solar cycle variation of mode area, we estimate the 'activity-free' area in synoptic maps corresponding to months 9–11 (low activity) and months 33–35 (high activity) by subtracting from the total area the portion with fields above a certain threshold times a filling factor. As threshold, we use the median value of 4 G of the high-activity synoptic maps. Using a filling factor of 0.18, derived by Title et al. (1992) for plages, the 'activity-free' area and as a consequence the acoustic energy is reduced by 3% from low to high activity. With an apparent area filling factor of 0.37, as derived by Lin & Rimmele (1999) for intranetwork fields, the 'activity-free' area is reduced by 7%. With these rough estimates, we find a variation of acoustic energy within a factor of two or less of the measured 6% reduction in mode area. Thus, it is plausible that the reduction in mode area is directly related to the increased number of flux tubes covering the solar surface during periods of high activity.

Elsworth et al. (1993) report a decrease in mode area of $35 \pm 5\%$ from solar minimum to maximum in the BISON data between 1981 and 1992. With $-1.75 \pm 0.37\%$/G for $l \leq 5$ (Figure 12) and a maximum difference of 16.7 G in NSO Kitt Peak magnetograms from 1981 to 1992, we estimate a decrease of $29 \pm 6\%$ between minimum and maximum, which is in good agreement with the BISON results given the different data sets and methods. The order and the sign is also in agreement with Pallé, Régulo, & Roca Cortés (1990a). Elsworth et al. (1993) found no significant variation with mode width, which is different from our result at higher l values. However, the level of significance is lower for mode width than for mode amplitude and area and the correlation with

sunspot numbers, as used by Elsworth et al. (1993), is slightly less significant than with magnetic flux. Using the average values in Table 2, we expect an increase in mode width of about 15% from solar minimum to maximum, but we have no good quantitative estimate for $l \leq 5$. An increase in line width would be in agreement with Pallé, Régulo, & Roca Cortés (1990b). However, if the mode width at this particular l range does not change with the solar cycle change, this would also lead to a low significance of the regression analysis.

The solar-cycle variation of the mode width reported by Meunier (1997) is the opposite of what we find and differs also from a previous analysis of South Pole data (Jefferies et al. 1990, 1991) which suggested a qualitative behavior similar to our results. Since she had only two South Pole data sets available and used a small subset of the $(l\nu)$ diagram, the difference might be a selection effect. Another possible explanation of the difference is that Meunier (1997) used an asymmetric line profile instead of a symmetric Lorentzian as in Jefferies et al. (1990, 1991) or in this study. The neglect of the line asymmetry might be important and influence the results.

Hindman, Haber, & Toomre (2000) report a strong shift in central mode frequency of up to 15 μHz in active regions versus the quiet Sun measured in the Dense-Pack data set from SOI/MDI devised for ring-diagram analysis. Since the behavior of active regions is dominated by magnetic fields as is the variation with the solar cycle and since it is well-known that sunspots absorb p-modes, we predict that the mode width in active regions is larger than in the quiet Sun and that the mode area is smaller. To make an approximate quantitative prediction, we assume that there is no l dependence of the variation in mode width and area up to the very high l values required for ring-diagram analysis ($l \sim 700$–1000), that the mode frequency shift continues to gradually increase with l at the rate of 1 nHz per degree for a 5 G change in the overall surface flux (Howe, Komm, & Hill 1999, for $l \leq 150$), and that mode width and area scale as the shift in central mode frequency. Under these assumptions, we predict for $l = 850$ a broadening in mode width of up to 38% in an active region and a reduction in mode area of up to 70% compared to the quiet Sun.

A decrease in mode energy of about 13% from solar minimum to maximum amounts to about 1×10^{30} erg s^{-1} using the order of magnitude estimate of the total energy flux flowing through p-modes calculated by Libbrecht (1988). The total (spectrally integrated) solar irradiance variation is about $\sim 0.1\%$ (Willson & Hudson 1988, 1991) between minimum and maximum corresponding to about 4×10^{30} erg s^{-1} in luminosity. Thus, the energy transferred from p-modes to flux tubes is large enough that it might contribute to the observed increase in irradiance with increasing activity. The irradiance variation is related to the presence of magnetic features (Lean 1997); dark sunspots reduce the local radiative output, whereas faculae, plages, and the network enhance the emission. But, to identify all sources of the solar irradiance cycle proves difficult. One question is whether brightness changes in magnetic features alone can account for the 11-yr variation or whether an additional non-facular global component (Kuhn, Libbrecht, & Dicke 1988) is needed. Recent studies indicate that magnetic features can account for the total variation (Lean et al. 1998; Chapman, Cookson, & Dobias 1996) and for the UV spectral variation (Lean et al. 1998). The energy transferred from p-modes to flux tubes would contribute to the magnetic component but

could also mimic a global brightness component. The UV radiation, which emerges from the middle photosphere, shows an order of magnitude larger variation than the total irradiance, which emerges predominantly from the visible surface. Modulation by upward extending flux tubes is suggested as a probable mechanism for these variations (Lean et al. 1998). Such a modulation could be excited by the interaction of flux tubes with p-modes.

The measurement of mode width, amplitude, and area and their temporal variation is made difficult by systematic effects in the data and limited understanding of mode physics. We attempt to adequately correct for systematic effects known to us and we are aware that the results might be improved by using asymmetric line profiles or by simultaneously studying velocity and intensity data. We finally point out that the available data cover only about one quarter of a solar cycle and that a reliable study of solar-cycle effects usually requires observations of at least one or two solar cycles.

This work was supported by NASA Grant S-92698-F. This work utilizes data obtained by the Global Oscillation Network Group (GONG) project, managed by the National Solar Observatory, a Division of the National Optical Astronomy Observatories, which is operated by AURA, Inc. under a cooperative agreement with the National Science Foundation. The data were acquired by instruments operated by the Big Bear Solar Observatory, High Altitude Observatory, Learmonth Solar Observatory, Udaipur Solar Observatory, Instituto de Astrofísico de Canarias, and Cerro Tololo Interamerican Observatory. The SOI–MDI project is supported by NASA grant NAG 5-3077 to Stanford University, with subcontracts to Lockheed Martin, to University of Colorado, and to Harvard University. SOHO is a mission of international cooperation between ESA and NASA. NSO/Kitt Peak data used here are produced cooperatively by NSF/NOAO, NASA/GSFC, and NOAA/SEL.

REFERENCES

Anderson, E.R., Duvall, Jr., T.L., & Jefferies, S.M. 1990, ApJ, 364, 699

Bachmann, K.T. & White, O.R. 1994, Sol. Phys., 150, 347

Balmforth, N.J. 1992, MNRAS, 255, 639

Bogdan, T.J., Hindman, B., Cally, P., & Charbonnneau, P. 1996, ApJ, 465, 406

Bogdan, T.J. & Zweibel, E.G. 1987, ApJ, 312, 444

Chapman, G.A., Cookson, A.M., & Dobias, J.J. 1996, J. Geophys. Res., 101, 13541

Elsworth, Y., Howe, R., Isaak, G.R., McLeod, C.P., Miller, B.A., New, R., Speake, C.C. & Wheeler, S.J. 1993, MNRAS, 265, 888

Elsworth, Y., Howe, R., Isaak, G.R., McLeod, C.P., Miller, B.A. et al. 1994, ApJ, 434, 801

Gershenfeld, N. 1999, The Nature of Mathematical Modeling, Cambridge University Press, Cambridge

Goldreich, P., Murray, N., & Kumar, P. 1994, ApJ, 424, 466

Gooode, P.R. & Strous, L.H. 1996, Bull. Astr. Soc. India, 24, 223

Goutte, C. 1997, Neural Computation, 9, 1245

Hasan, S.S. 1997, ApJ, 480, 803

Hasan, S.S. & Kalkofen, W. 1998, PASP, 154, CD-767

Hill, F., Stark, P.B., Stebbins, R.T., Anderson, E.R, Brown, T.M. et al. 1996, Science, 272, 1292

Hill, F., Anderson, E., Howe, R., Jefferies, S.M., Komm, R.W., & Toner, C.G. 1998, Dynamics of the Interior of the Sun and Sun-like Stars (Eds. S.G. Korzennik & A. Wilson), ESA SP-418, ESA Publications Division, Noordwijk, The Netherlands, 1998, 231

Hindman, B.W., Haber, D.A., & Toomre, J. 2000, SOHO 9 Workshop (Eds. T.L. Duvall & A.G. Kosovichev), Sol. Phys., (submitted)

Howe, R., Komm, R., & Hill, F. 1999, ApJ, 524, 1084

Howe, R., Komm, R., & Hill, F. 2000, SOHO 9 Workshop (Eds. T.L. Duvall & A.G. Kosovichev), Sol. Phys., (submitted)

Jefferies, S.M., Duvall, Jr., T.L., Harvey, J.W., & Pomerantz, M.A. 1990, in Osaki Y., Shibahashi H., eds, Progress of Seismology of the Sun and Stars, Springer-Verlag, Berlin, p. 135

Jefferies, S.M., Duvall, Jr., T.L., Harvey, J.W., Osaki, Y., & Pomerantz, M.A. 1991, ApJ, 377, 330

Keppens, R., Bogdan, T.J., & Goossens, M. 1994, ApJ, 436, 372

Komm, R.W., Anderson, E., Hill, F. & Howe, R. 1999, Temporal Window Correction of Mode Width and Amplitude, GONG Technote `http://www.nso.noao.edu/nsokp/dataarch.html`

Korzennik, S.G. 1990, Ph.D thesis, Univ. California, Los Angeles

Kuhn, J.R., Libbrecht, K.G., & Dicke, R.H. 1988, Science, 242, 908

Lean, J. 1997, ARA&A, 35, 33

Lean, J.L., Cook, J., Marquette, W., & Johannesson, A. 1998, ApJ, 492, 390

Libbrecht, K.G. 1988, ApJ, 334, 510

Libbrecht, K.G. & Woodard, M.F. 1990, Nature, 345, 779

Lin, H. & Rimmele, T., 1999, ApJ, 514, 448

Meunier, N. 1997, Ph.D Thesis Université D. Diderot, Diagnostics observationels du champ magnétique solaire: distribution spatiale, dynamique et processus de génération

Nesis, A., Hammer, R., Hanslmeier, A., Schleicher, H., Sigwarth, M., & Staiger, J. 1996, A&A, 310, 973

Osaki, Y. 1990, in Osaki Y., Shibahashi H., eds, Progress of Seismology of the Sun and Stars, Springer-Verlag, Berlin, p. 75

Pallé, P.L., Régulo, C., & Roca Cortés, T. 1990, in Osaki Y., Shibahashi H., eds, Progress of Seismology of the Sun and Stars, Springer-Verlag, Berlin, p. 129

Pallé, P.L., Régulo, C., & Roca Cortés, T. 1990, in Osaki Y., Shibahashi H., eds, Progress of Seismology of the Sun and Stars, Springer-Verlag, Berlin, p. 189

Pintèr, B. & Goossens, M. 1999, A&A, 347, 321

Rast, M.P. 1999, ApJ, (submitted)

Rimmele, T.R., Goode, P.H., Harold, E. & Stebbins, R.T. 1995, ApJ, 444, 119L

Ryutova, M.P. & Priest, E.R. 1993, ApJ, 419, 349

Ryutova, M.P. & Priest, E.R. 1993, ApJ, 419, 371

Title, A., Topka, K., Tarbell, T., Schmidt, W., & Balke, C. 1992, ApJ, 393, 782

Toomre, J., et al. 2000, SOHO 9 Workshop (Eds. T.L. Duvall & A.G. Kosovichev), Sol. Phys., (submitted)

Willson, R.C. & Hudson, H.S. 1988, Nature, 332, 810

Willson, R.C. & Hudson, H.S. 1991, Nature, 351, 42

Fig. 1.— Solar magnetic activity during GONG months 1 to 35. Each point represents the central month of a GONG 3-month time series.

Fig. 2.— An example of the (m/l) variation of mode width, Γ, amplitude, A, mode area, $\Gamma * A$, and background amplitude, b_0. The data are normalized by the values at $m = 0$.

Fig. 3.— Examples of the variation of Γ with fill factor for the same l but different n values for undeconvolved GONG data ($\times$), SOI data ($\diamond$), and deconvolved GONG data ($\square$). The solid line is a linear fit to the undeconvolved GONG data.

Fig. 4.— The average in-sample error ($\times$) and out-of-sample error ($\square$) of polynomial fits of Γ as a function of fill factor for different degrees of the fitting polynomials. The top panel shows the results for randomly dividing the data set into two subsets of about equal size, while the bottom panel shows the results for excluding from the fit the four data points with the largest fill factors.

Fig. 5.— The slopes normalized by the intercepts of a linear fit of mode width versus fill factor (Equation 1) as a function of l and ν. The units are percent per $(1. - fill)$.

Fig. 6.— Mode width extraploated to 100% fill.

Fig. 7.— Example of the variation of Γ, A, $\Gamma \times A$, and b_0 with magnetic activity for a single multiplet $(l = 50, n = 9)$. Activity measures are magnetic flux (dashed line) and sunspot numbers (dotted line). The values were corrected for the fill factor and normalized by the corresponding extrapolated value at 100% fill and minimum level of activity.

Fig. 8.— The average in-sample error ($\times$) and out-of-sample error ($\square$) of polynomial fits of Γ as a function of magnetic activity for different degrees of the polynomials. The activity measures used are magnetic flux (top panel) and sunspot number (bottom panel).

Fig. 9.— Correlation coefficients of multi-linear regression in fill factor ($\times$) and magnetic activity ($\square$) for mode width. The two horizontal lines are the 95% and 99.9% significance level.

Fig. 10.— The slopes of the linear regression of mode width versus magnetic activity (Equation 2) as a function of l and ν normalized by the intercept. Included are rebinned and averaged values with a binsize of 5 in l (top panel) and a binsize of 100μHz (bottom panel). The error bars represent the standard error of the mean; the dotted lines indicate ± 1 standard deviation. The units are percent per Gauss.

Fig. 11.— As Figure 10, but for mode amplitude (measured at $(m/l) = 1$).

Fig. 12.— As Figure 10, but for mode area (measured at $(m/l) = 1$).

Fig. 13.— As Figure 10, but for background amplitude (measured at $(m/l) = 1$). Included are rebinned and averaged values with a binsize of 9 in l for two regions of the $(l\nu)$ diagram ($\square$: $l \geq 80$ and $\nu \geq 3$ mHz, $\times$: $l < 80$ or $\nu < 3$ mHz. Top panel: all available multiplets, Bottom panel:

limited to multiplets where the regression leads to a $\geq 95\%$ level of significance.

Fig. 14.— A distribution of slopes determined from fitting 1000 random samples, where the magnetic field strength values are randomly assigned in each sample, averaged over all multiplets for $l \geq 30$. The bottom x-axes are normalized by the standard deviations of the distributions, while the top x-axes are in the same units as the y-axes in Figures 10–13. The dotted lines indicate the means of the distributions, while the dashed lines indicate the average slopes of the actual measurements (Figures 10–13).

Fig. 15.— Mode area slopes as a function of the correlation between the randomized magnetic field and the measured magnetic field (top row) and between the randomized magnetic field and the fill factor (bottom row) for all frequencies (left column) and for the frequency range from 2.7 to 3.3 mHz (right column) for $l \geq 30$. The square symbols indicate the actual measurements.

Fig. 16.— A comparison of normalized slopes of good fits common to the regression in magnetic flux and to the one in sunspot numbers. The solid lines indicate linear fits between the two data sets.

Table 1. GONG time series used in this work. The average magnetic flux was derived from NSO Kitt Peak synoptic maps. The sunspot numbers are from the NSO Sacramento Peak archive.

Months	Start	Stop	Fill	Flux (G)	Sunspot #
1–3	95-05-07	95-08-22	0.8088	4.951	13.8
2–4	95-06-12	95-09-27	0.8189	4.810	13.9
3–5	95-07-18	95-11-02	0.8501	4.822	16.6
4–6	95-08-23	95-12-08	0.8602	4.832	14.2
5–7	95-09-28	96-01-13	0.8800	4.753	13.9
6–8	95-11-03	96-02-18	0.8800	4.421	8.8
7–9	95-12-09	96-03-25	0.8918	4.139	8.8
8–10	96-01-14	96-04-30	0.9007	3.989	6.2
9–11	96-02-19	96-06-05	0.9195	3.969	6.0
10–12	96-03-26	96-07-11	0.8817	4.013	7.1
11–13	96-05-01	96-08-16	0.8244	4.196	8.9
12–14	96-06-06	96-09-21	0.7696	4.276	8.5
13–15	96-07-12	96-10-27	0.8019	4.297	4.9
14–16	96-08-17	96-12-02	0.8692	4.309	5.5
15–17	96-09-22	97-01-07	0.9219	4.519	6.7
16–18	96-10-28	97-02-12	0.9234	4.619	7.8
17–19	96-12-03	97-03-20	0.9099	4.529	6.7
18–20	97-01-08	97-04-25	0.8670	4.340	7.8
19–21	97-02-13	97-05-31	0.8251	4.345	10.9
20–22	97-03-21	97-07-06	0.8093	4.457	12.3
21–23	97-04-26	97-08-11	0.8298	4.483	12.0
22–24	97-06-01	97-09-16	0.8238	4.859	17.6
23–25	97-07-07	97-10-22	0.8339	5.341	23.2
24–26	97-08-12	97-11-27	0.7982	5.945	30.1
25–27	97-09-17	98-01-02	0.8176	6.372	29.9
26–28	97-10-23	98-02-07	0.8000	6.609	31.6
27–29	97-11-28	98-03-15	0.8550	6.826	33.6
28–30	98-01-03	98-04-20	0.8412	7.294	39.4
29–31	98-02-08	98-05-26	0.8251	7.267	42.1
30–32	98-03-16	98-07-01	0.8036	7.789	47.4
31–33	98-04-21	98-08-06	0.7818	8.270	51.6
32–34	98-05-27	98-09-11	0.7972	9.310	62.5
33–35	98-07-02	98-10-17	0.8000	9.862	67.0

Table 1—Continued

Months	Start	Stop	Fill	Flux (G)	Sunspot #

Table 2. Normalized slopes in percent per Gauss of a linear regression of mode parameters versus magnetic activity averaged over all multiplets for (a) all l and ν, (b) all l and $2.7 \leq \nu \leq 3.3$ mHz, (c) $l \geq 30$ and all ν, and (d) $l \geq 30$ and $2.7 \leq \nu \leq 3.3$ mHz. The table shows the mean slope, the standard deviation, the number of multiplets, and σ, the mean divided by the standard deviation of the distribution of 1,000 randomized data sets.

Parameter	(a) Mean	Stddev	Num	σ	(b) Mean	Stddev	Num	σ
Γ	0.524	0.646	682	2.9	0.769	0.679	232	3.1
$A\,(m/l=0)$	–0.723	0.723	694	–3.9	–0.794	0.721	206	–3.4
$A\,(m/l=1)$	–1.206	0.925	637	–4.8	–1.561	0.977	207	–4.6
$\Gamma \times A\ (0)$	–0.664	0.521	706	–4.9	–0.819	0.550	207	–5.0
$\Gamma \times A\ (1)$	–0.971	0.692	524	–5.0	–1.317	0.747	152	–5.1
$b_0\,(m/l=0)$	–0.390	1.796	395	–1.0	–0.790	1.555	127	–1.9
$b_0\,(m/l=1)$	0.423	2.687	311	0.5	–0.412	2.300	96	–0.5
Parameter	(c) Mean	Stddev	Num	σ	(d) Mean	Stddev	Num	σ
Γ	0.499	0.617	599	2.7	0.746	0.652	196	2.9
$A\,(m/l=0)$	–0.670	0.627	585	–3.6	–0.722	0.608	171	–3.2
$A\,(m/l=1)$	–1.140	0.795	522	–4.7	–1.466	0.851	169	–4.4
$\Gamma \times A\ (0)$	–0.613	0.453	538	–4.8	–0.753	0.480	152	–4.8
$\Gamma \times A\ (1)$	–0.922	0.633	397	–4.9	–1.272	0.697	105	–5.0
$b_0\,(m/l=0)$	–0.613	1.017	205	–1.5	–0.977	0.725	61	–2.2
$b_0\,(m/l=1)$	0.366	2.206	182	0.4	–0.322	1.428	53	–0.3

Table 3. As Table 2, but excluding all values with $l > 80$ and $\nu > 3.0$ mHz to reduce the influence of potentially overestimated background amplitudes (see Figure 13).

Parameter	(a)	Mean	Stddev	Num	σ	(b)	Mean	Stddev	Num	σ
Γ		0.428	0.660	373	2.2		0.583	0.727	111	2.4
$A\,(m/l=0)$		–0.857	0.800	367	–4.0		–0.791	0.808	91	–3.5
$A\,(m/l=1)$		–1.297	0.987	323	–4.6		–1.476	0.938	97	–4.1
$\Gamma \times A\ (0)$		–0.722	0.555	392	–5.1		–0.829	0.542	94	–5.2
$\Gamma \times A\ (1)$		–1.134	0.725	269	–4.9		–1.179	0.738	74	–4.7
$b_0\,(m/l=0)$		–0.791	0.984	235	–1.9		–0.878	1.217	66	–1.9
$b_0\,(m/l=1)$		–0.072	1.276	150	–0.1		–0.216	1.708	52	–0.2
Parameter	(c)	Mean	Stddev	Num	σ	(d)	Mean	Stddev	Num	σ
Γ		0.413	0.642	341	2.1		0.559	0.713	94	2.3
$A\,(m/l=0)$		–0.797	0.687	315	–3.8		–0.709	0.704	75	–3.3
$A\,(m/l=1)$		–1.107	0.777	269	–4.4		–1.389	0.802	78	–3.9
$\Gamma \times A\ (0)$		–0.654	0.466	289	–4.8		–0.767	0.467	63	–5.0
$\Gamma \times A\ (1)$		–1.038	0.626	202	–4.8		–1.128	0.695	50	–4.7
$b_0\,(m/l=0)$		–0.986	0.669	122	–2.2		–1.078	0.678	32	–2.2
$b_0\,(m/l=1)$		0.055	1.040	84	0.1		–0.055	1.389	29	–0.1

Table 4. As Table 2, but for sunspot numbers. The normalized slopes are in percent per sunspot number.

Parameter	(a)	Mean	Stddev	Num	σ	(b)	Mean	Stddev	Num	σ
Γ		0.0415	0.0618	697	2.5		0.0647	0.0637	232	2.8
$A\,(m/l=0)$		–0.0638	0.0701	730	–3.7		–0.0729	0.0699	209	–3.4
$A\,(m/l=1)$		–0.1118	0.0895	667	–4.8		–0.1460	0.0962	212	–4.7
$\Gamma \times A\ (0)$		–0.0611	0.0512	749	–4.8		–0.0777	0.0541	215	–5.1
$\Gamma \times A\ (1)$		–0.0927	0.0665	552	–5.1		–0.1278	0.0727	155	–5.3
$b_0\,(m/l=0)$		–0.0280	0.1589	483	–0.7		–0.0591	0.1395	161	–1.6
$b_0\,(m/l=1)$		0.0232	0.2146	491	0.3		–0.0346	0.1895	169	–0.4
Parameter	(c)	Mean	Stddev	Num	σ	(d)	Mean	Stddev	Num	σ
Γ		0.0391	0.0588	611	2.3		0.0627	0.0613	196	2.6
$A\,(m/l=0)$		–0.0659	0.1049	618	–3.4		–0.1153	0.0978	173	–3.1
$A\,(m/l=1)$		–0.1058	0.0771	543	–4.7		–0.1373	0.0836	172	–4.5
$\Gamma \times A\ (0)$		–0.0558	0.0847	568	–4.7		–0.1089	0.0886	157	–5.0
$\Gamma \times A\ (1)$		–0.0885	0.0609	417	–5.0		–0.1236	0.0683	107	–5.3
$b_0\,(m/l=0)$		–0.0495	0.1880	259	–1.1		–0.1120	0.1703	85	–1.7
$b_0\,(m/l=1)$		0.0183	0.1727	331	0.2		–0.0283	0.1319	116	–0.2

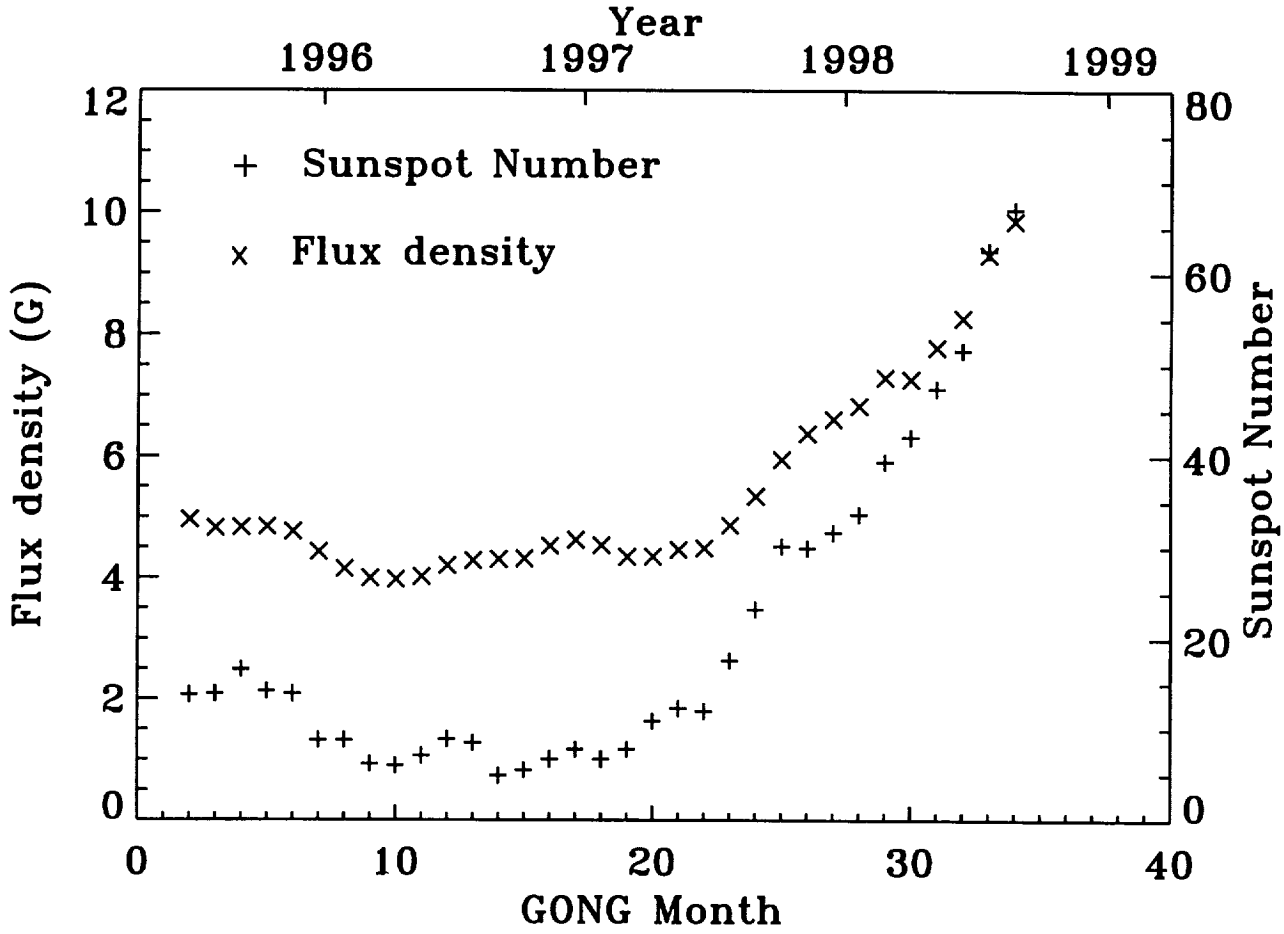
Year
1996
1997
1998
1999
+ Sunspot Number
× Flux density
Flux density (G)
Sunspot Number
GONG Month
0
2
4
6
8
10
12
0
20
40
60
80
0
10
20
30
40

Fig. 1

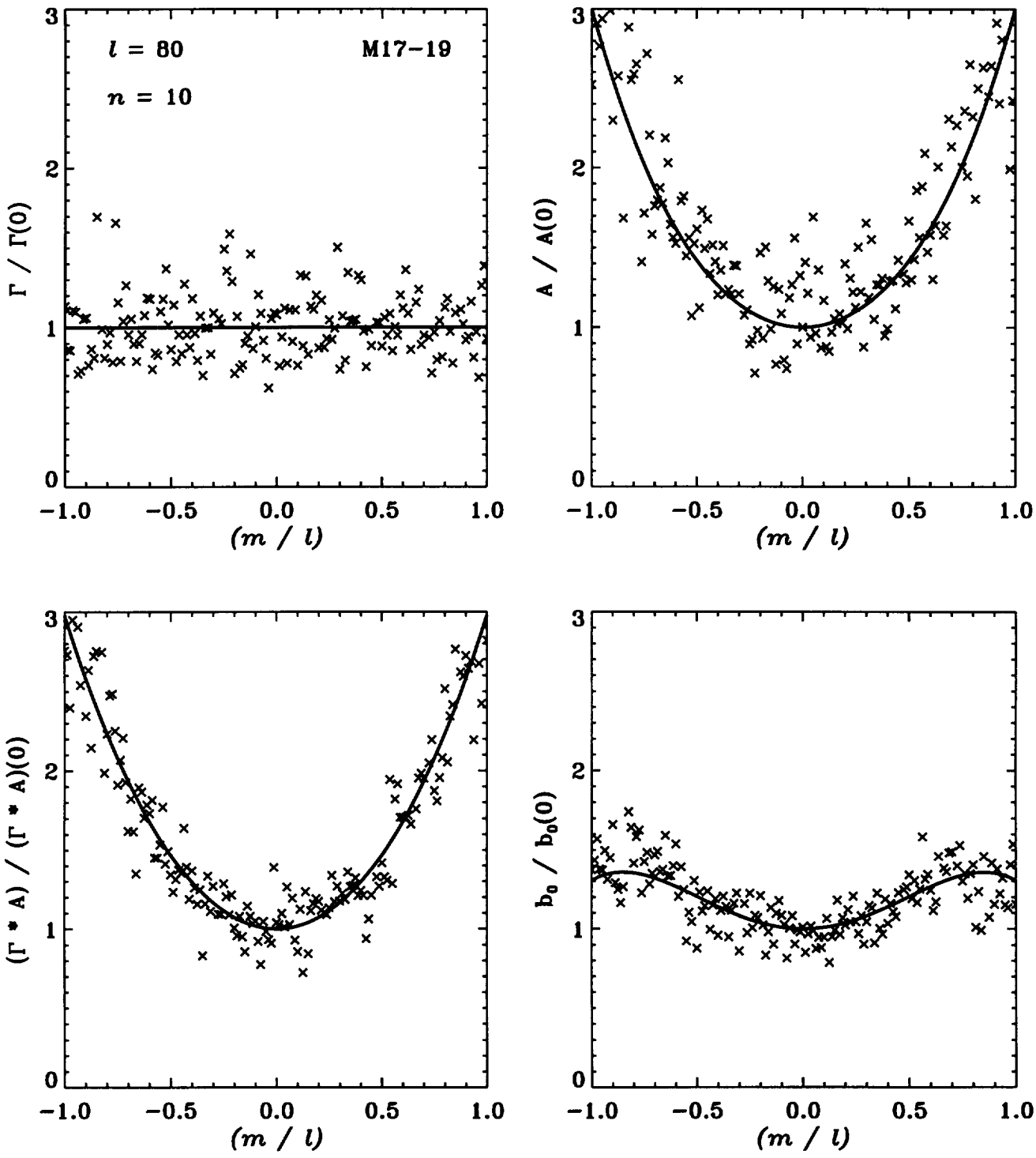

Fig. 2

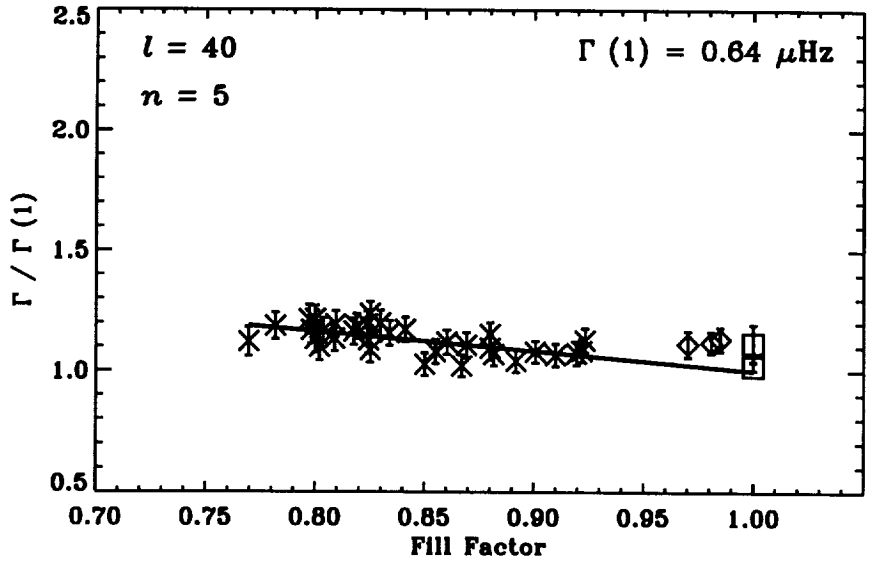
l = 40
n = 5
Γ (1) = 0.64 μHz
Γ / Γ (1)
Fill Factor
2.5
2.0
1.5
1.0
0.5
0.70
0.75
0.80
0.85
0.90
0.95
1.00

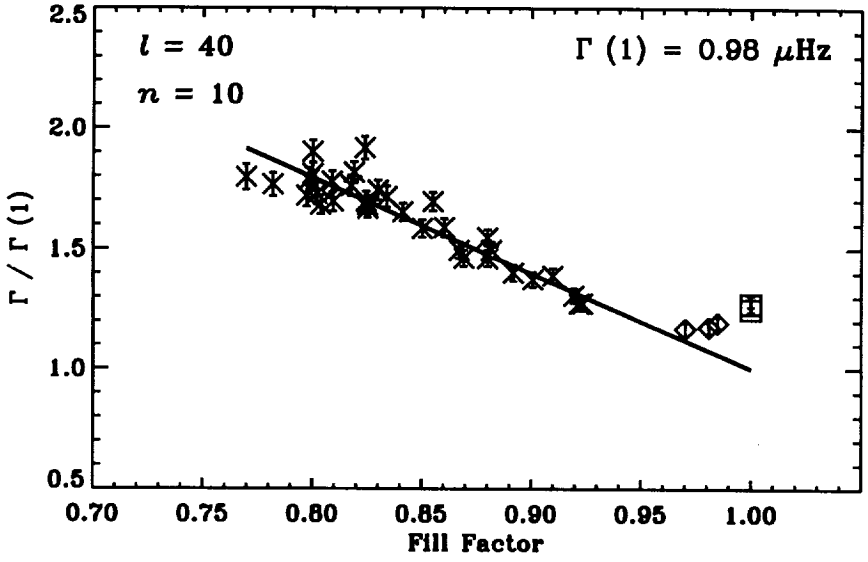
l = 40
n = 10
Γ (1) = 0.98 μHz
Γ / Γ (1)
Fill Factor
2.5
2.0
1.5
1.0
0.5
0.70
0.75
0.80
0.85
0.90
0.95
1.00

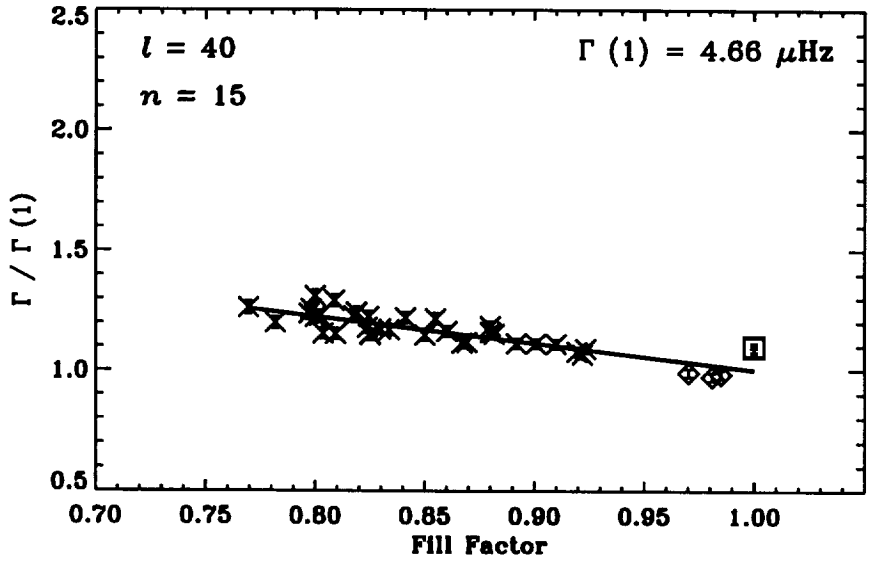
l = 40
n = 15
Γ (1) = 4.66 μHz
Γ / Γ (1)
Fill Factor
2.5
2.0
1.5
1.0
0.5
0.70
0.75
0.80
0.85
0.90
0.95
1.00

Fig. 3

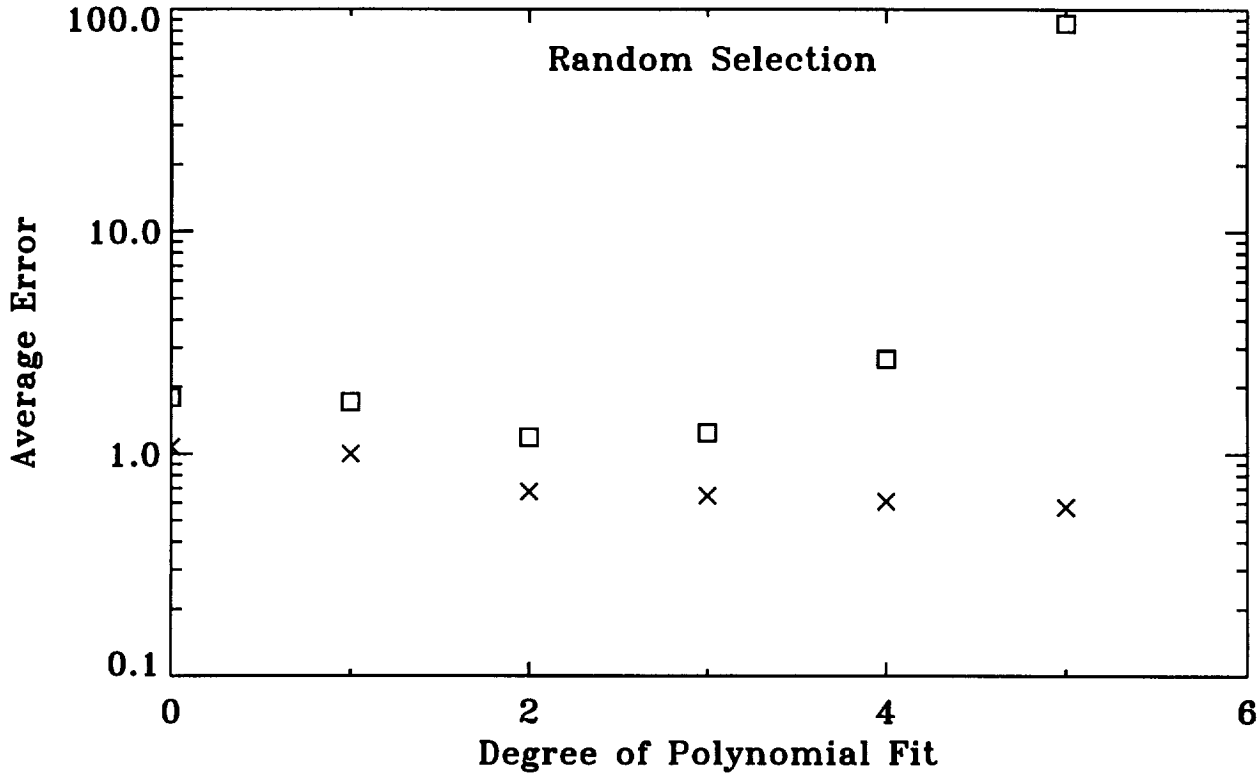
Random Selection
100.0
10.0
1.0
0.1
Average Error
0
2
4
6
Degree of Polynomial Fit

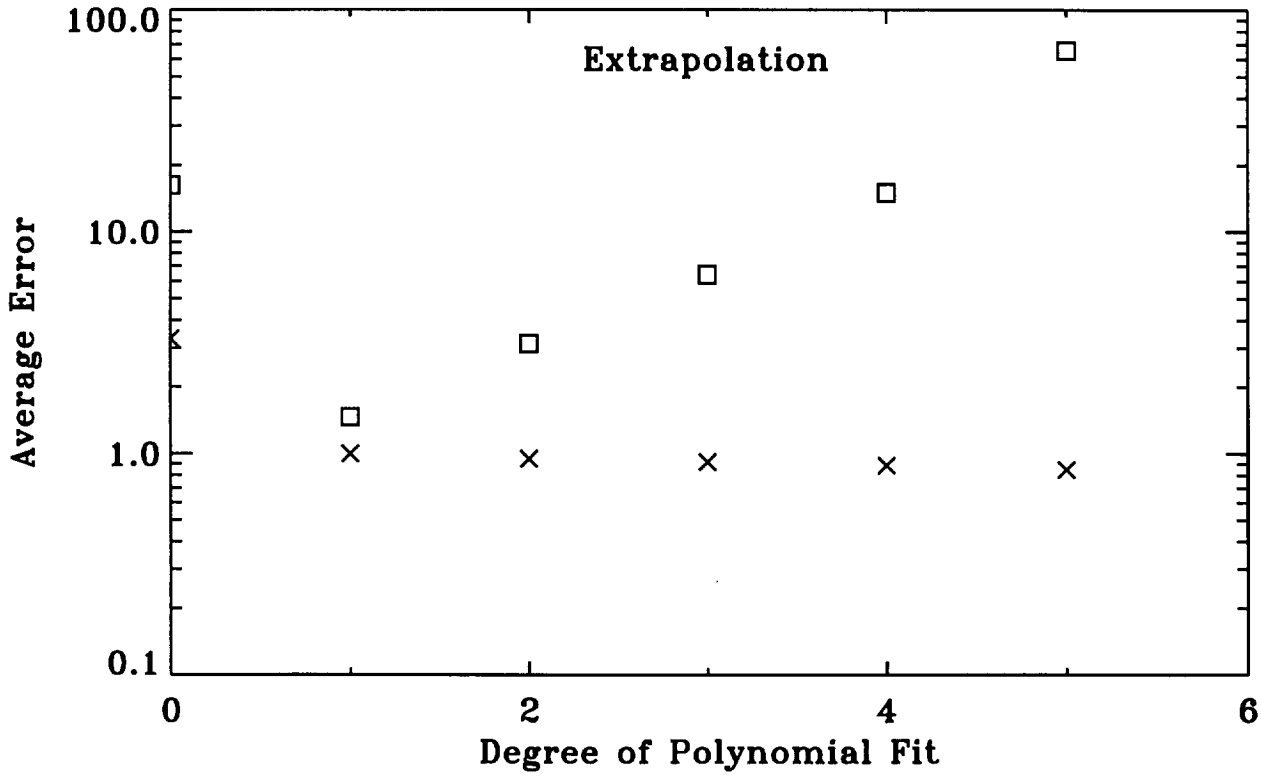
Extrapolation
100.0
10.0
1.0
0.1
Average Error
0
2
4
6
Degree of Polynomial Fit

Fig. 4

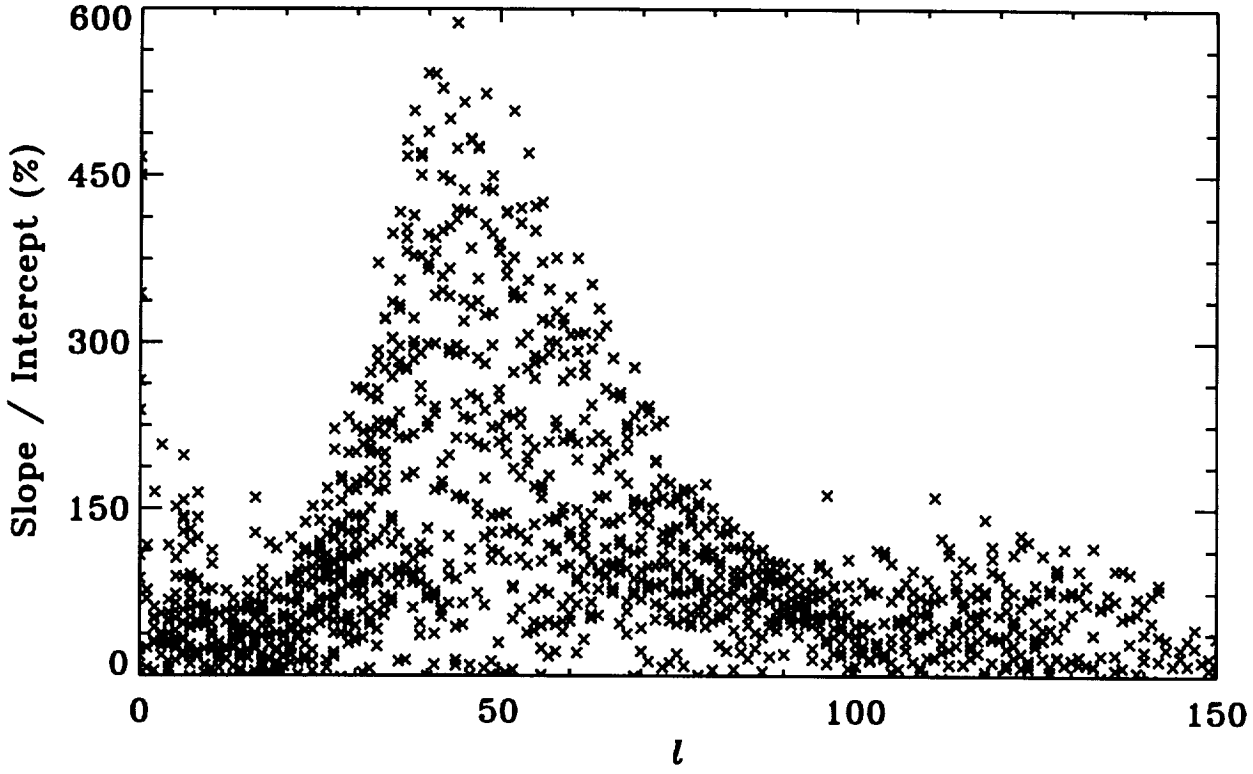
600
450
300
150
0
Slope / Intercept (%)
0
50
100
150
l

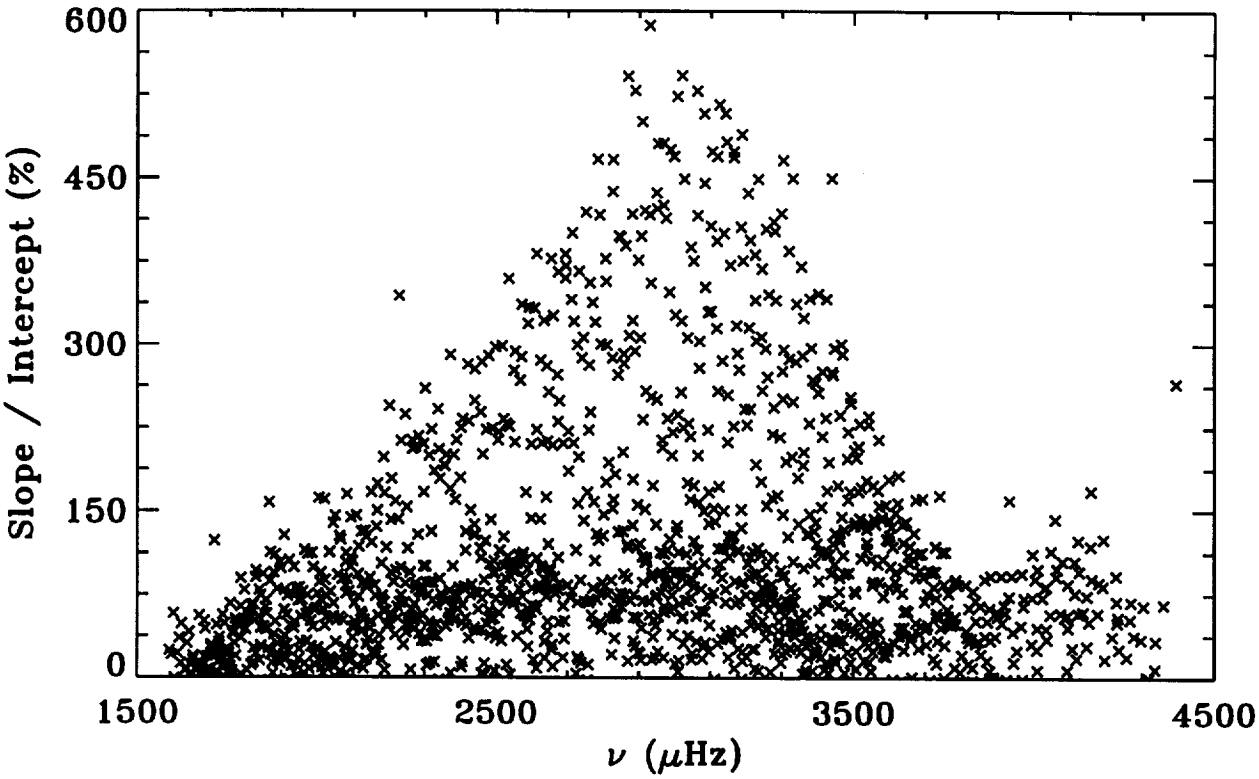
600
450
300
150
0
Slope / Intercept (%)
1500
2500
3500
4500
ν (μHz)

Fig.5

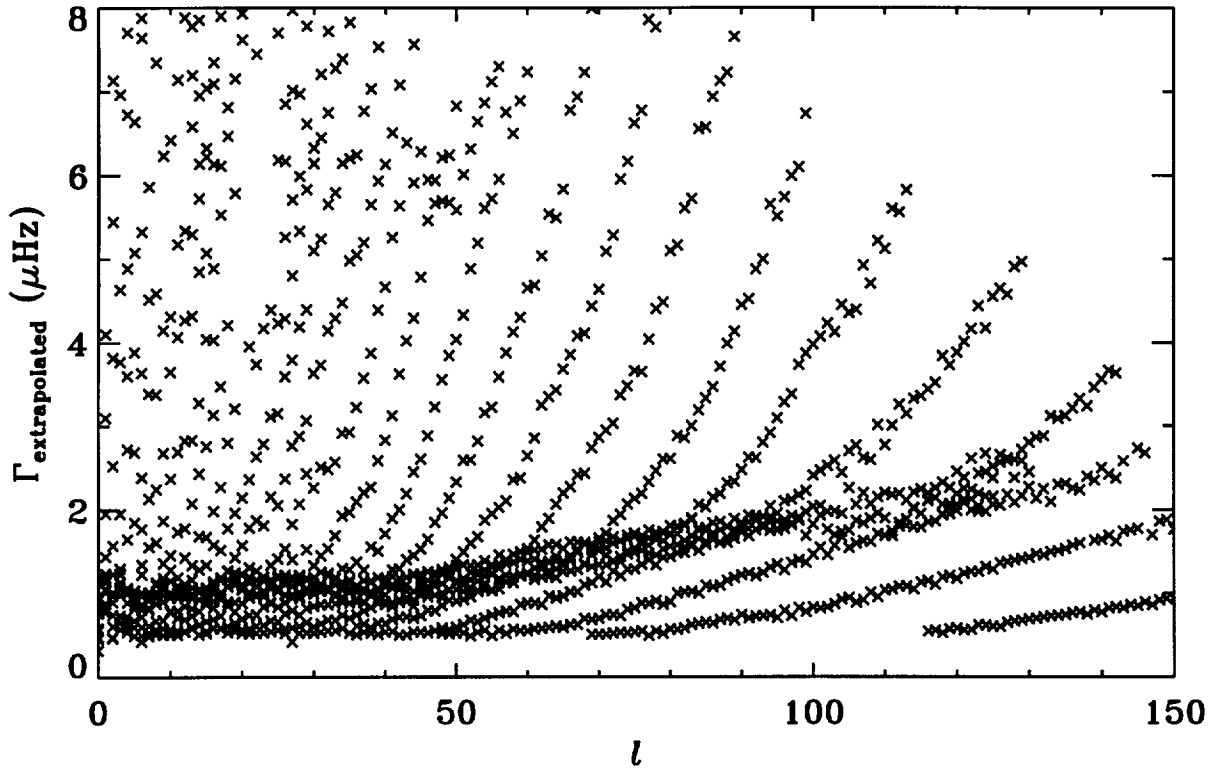
8
6
4
2
0
$\Gamma_{extrapolated}$ (μHz)
0
50
100
150
l

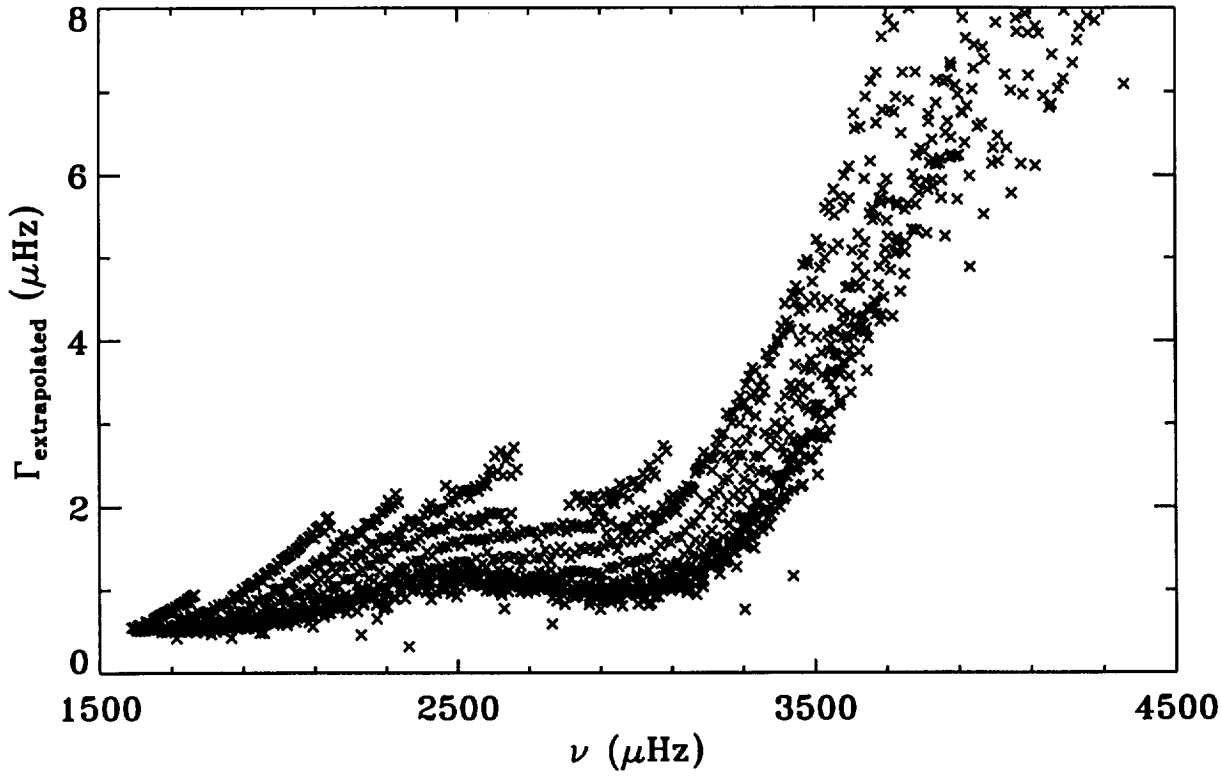
8
6
4
2
0
$\Gamma_{extrapolated}$ (μHz)
1500
2500
3500
4500
ν (μHz)

Fig. 6

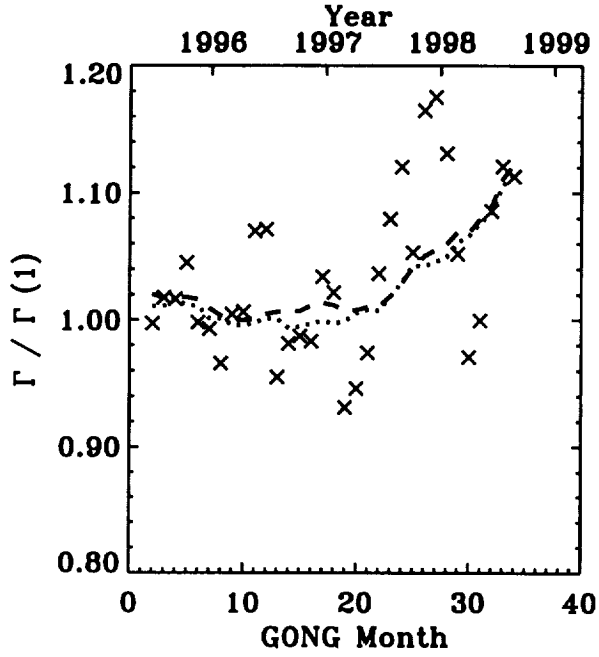
Year
1996
1997
1998
1999
1.20
1.10
1.00
0.90
0.80
Γ / Γ (1)
0
10
20
30
40
GONG Month

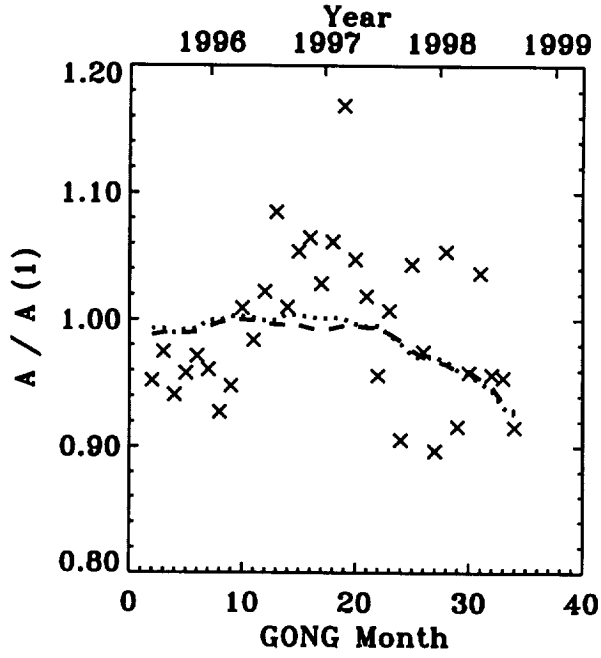
Year
1996
1997
1998
1999
1.20
1.10
1.00
0.90
0.80
A / A (1)
0
10
20
30
40
GONG Month

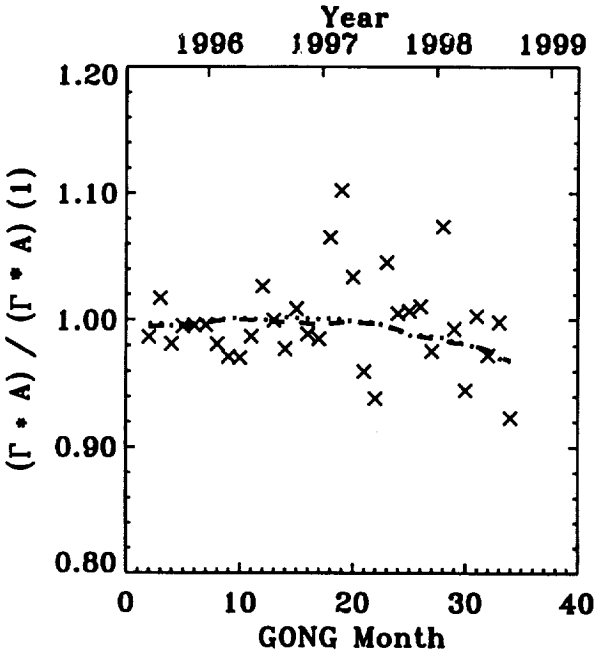
Year
1996
1997
1998
1999
1.20
1.10
1.00
0.90
0.80
(Γ * A) / (Γ * A) (1)
0
10
20
30
40
GONG Month

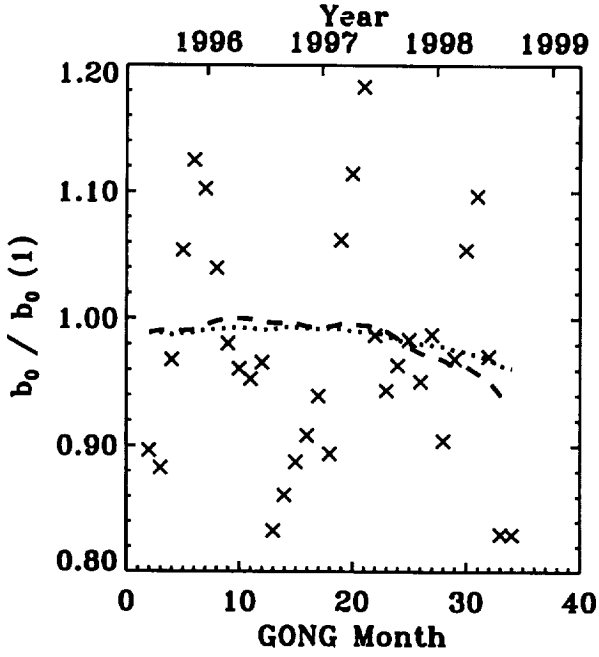
Year
1996
1997
1998
1999
1.20
1.10
1.00
0.90
0.80
b0 / b0 (1)
0
10
20
30
40
GONG Month

Fig.7

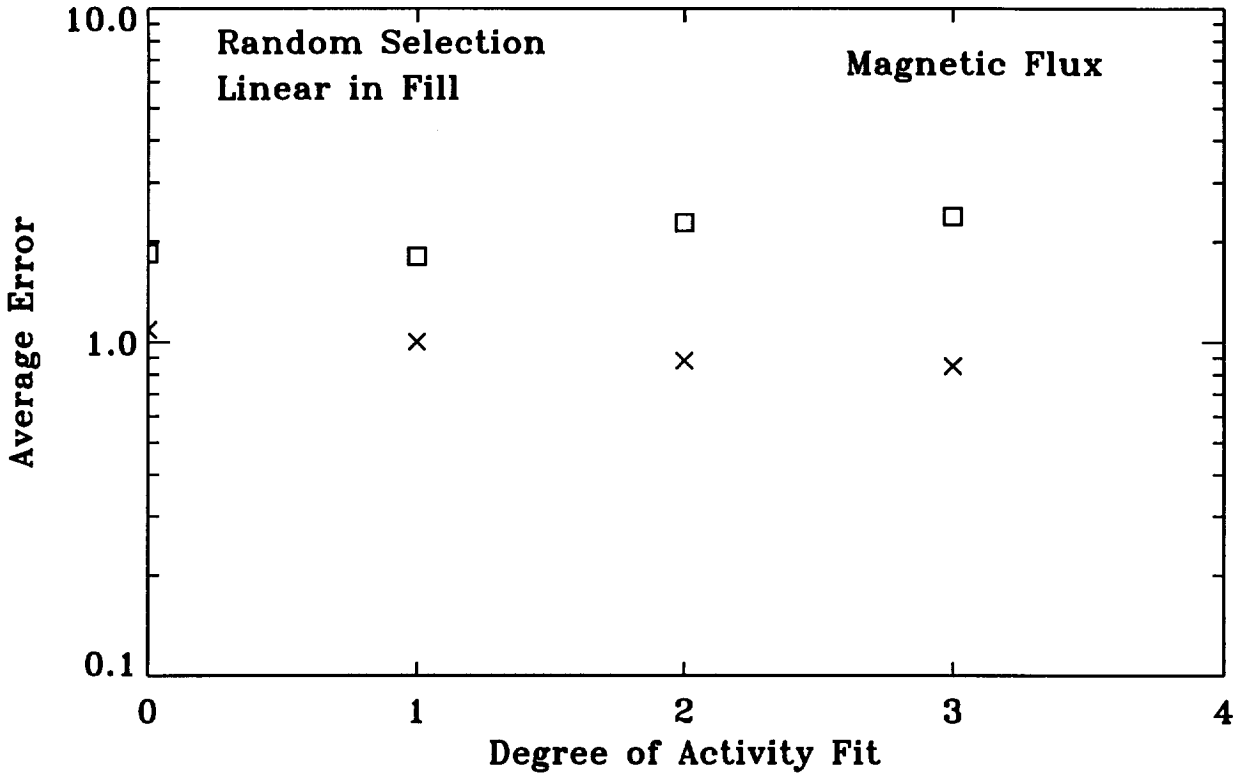
Random Selection
Linear in Fill
Magnetic Flux
Average Error
10.0
1.0
0.1
0
1
2
3
4
Degree of Activity Fit

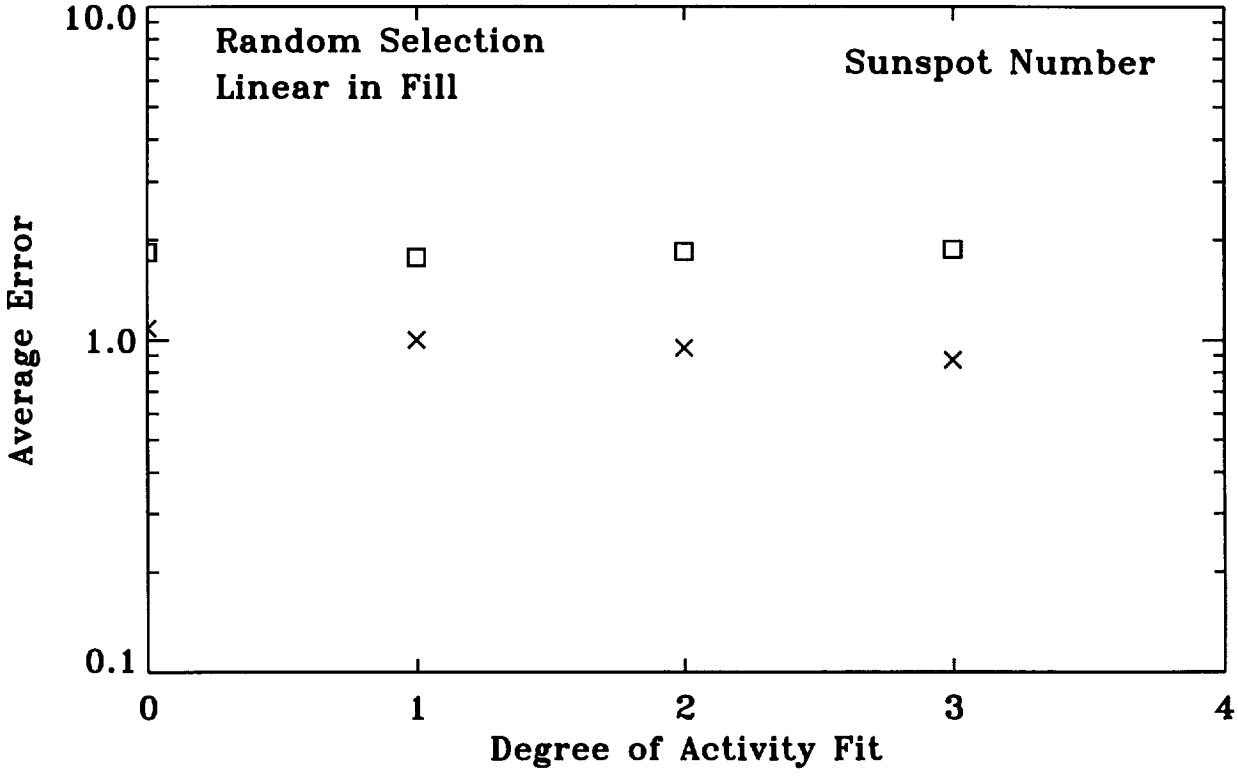
Random Selection
Linear in Fill
Sunspot Number
Average Error
10.0
1.0
0.1
0
1
2
3
4
Degree of Activity Fit

Fig. 8

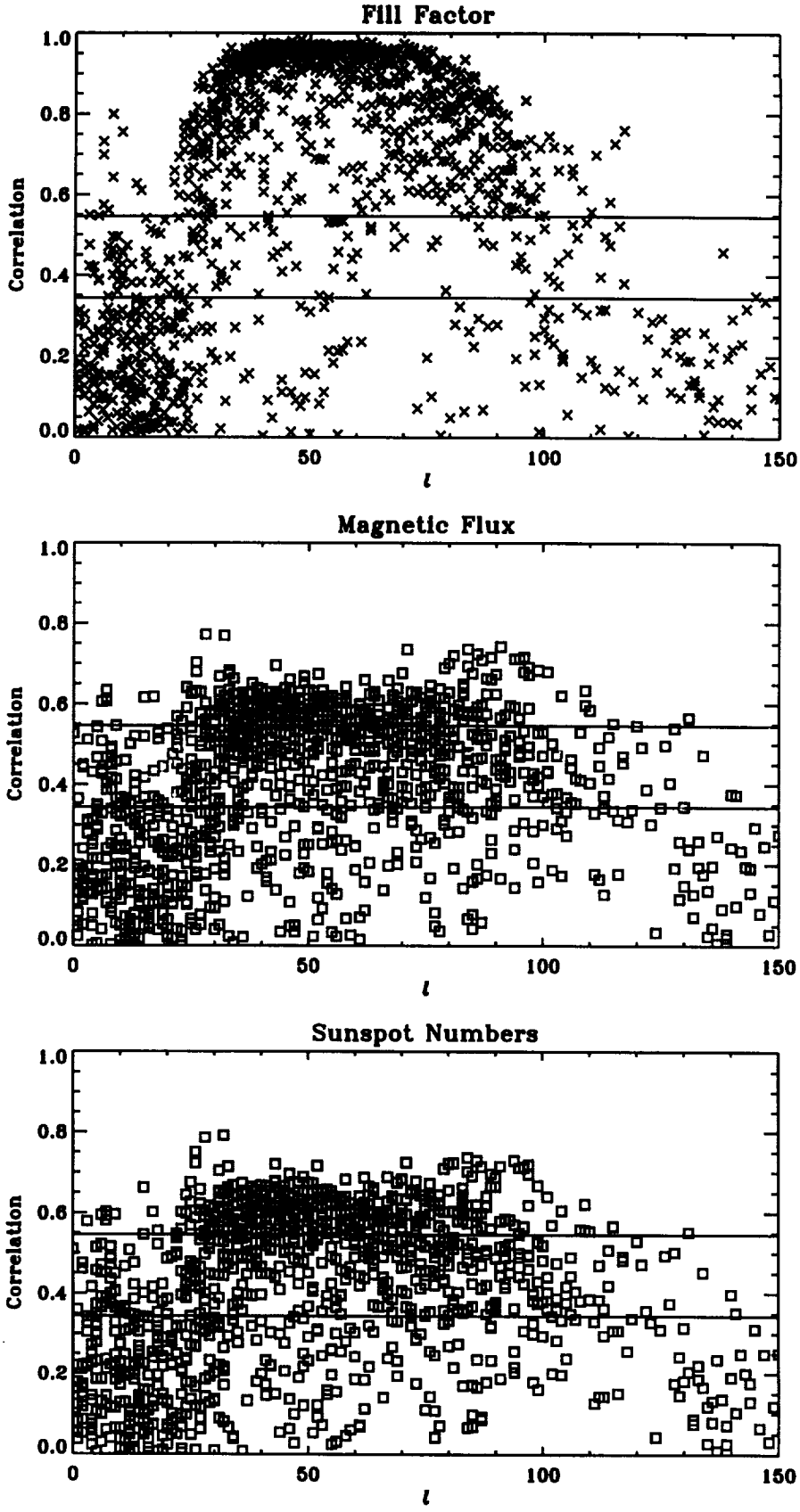
Fill Factor
Correlation
1.0
0.8
0.6
0.4
0.2
0.0
0
50
100
150
l
Magnetic Flux
Correlation
1.0
0.8
0.6
0.4
0.2
0.0
0
50
100
150
l
Sunspot Numbers
Correlation
1.0
0.8
0.6
0.4
0.2
0.0
0
50
100
150
l

Fig. 9

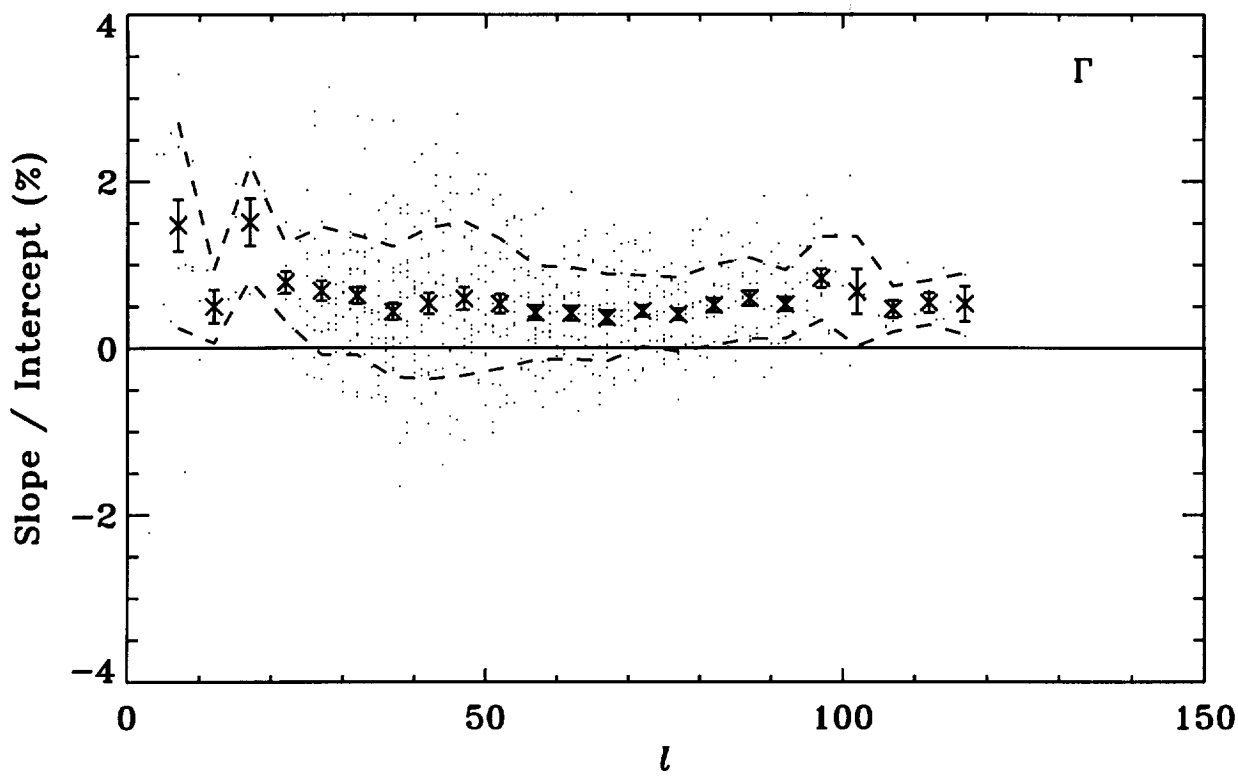
Γ
Slope / Intercept (%)
4
2
0
−2
−4
0
50
100
150
l

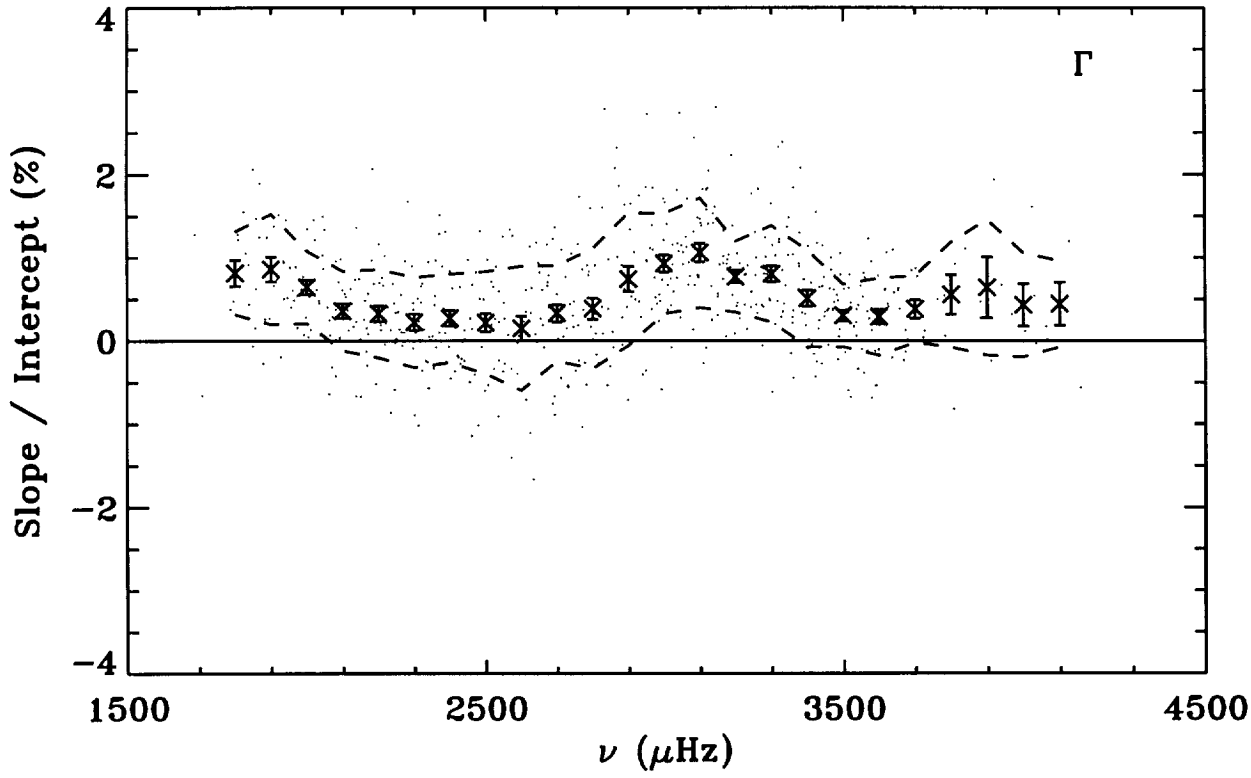
Γ
Slope / Intercept (%)
4
2
0
−2
−4
1500
2500
3500
4500
ν (μHz)

Fig. 10

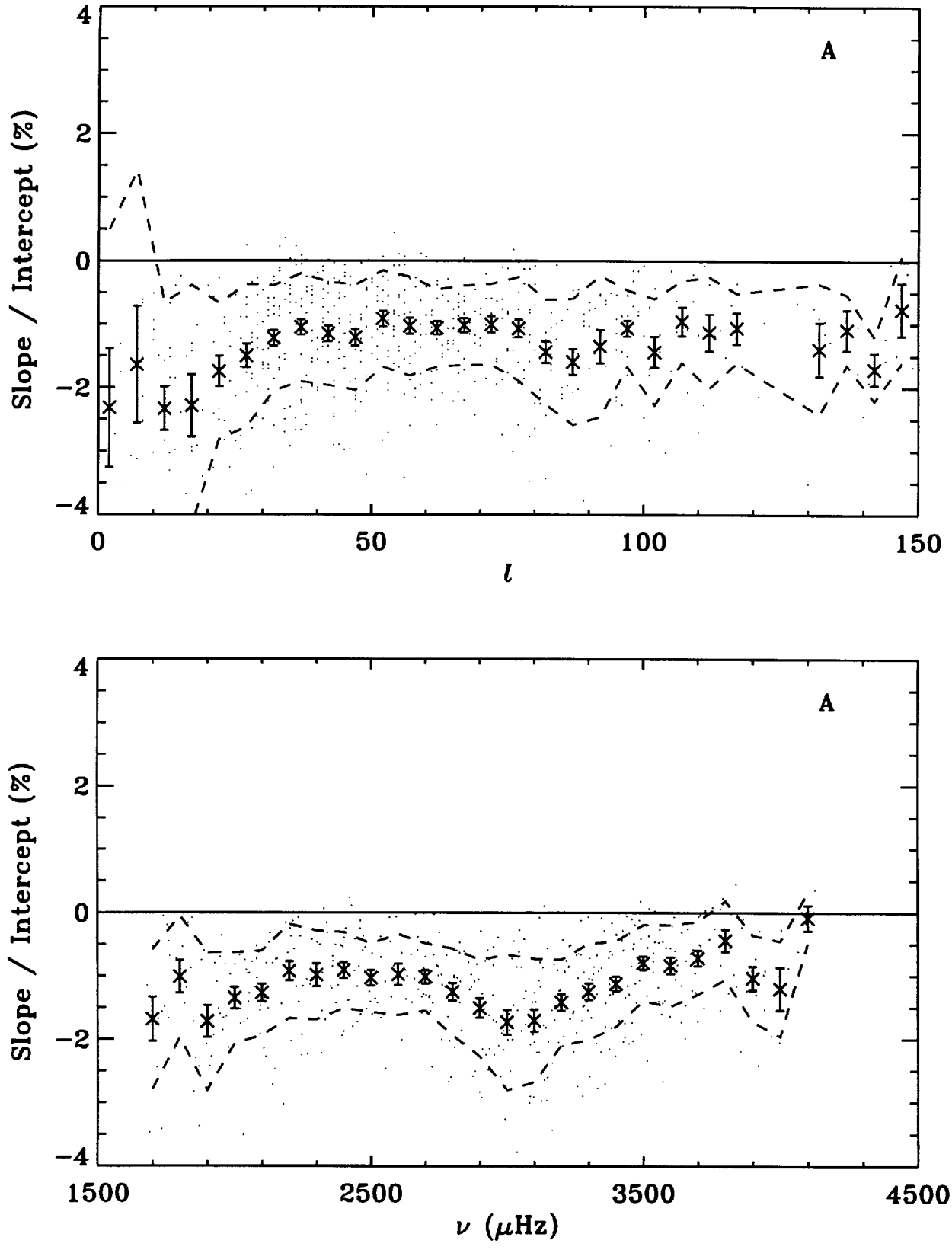
A
Slope / Intercept (%)
4
2
0
−2
−4
0
50
100
150
l
A
Slope / Intercept (%)
4
2
0
−2
−4
1500
2500
3500
4500
ν (μHz)

Fig. 11

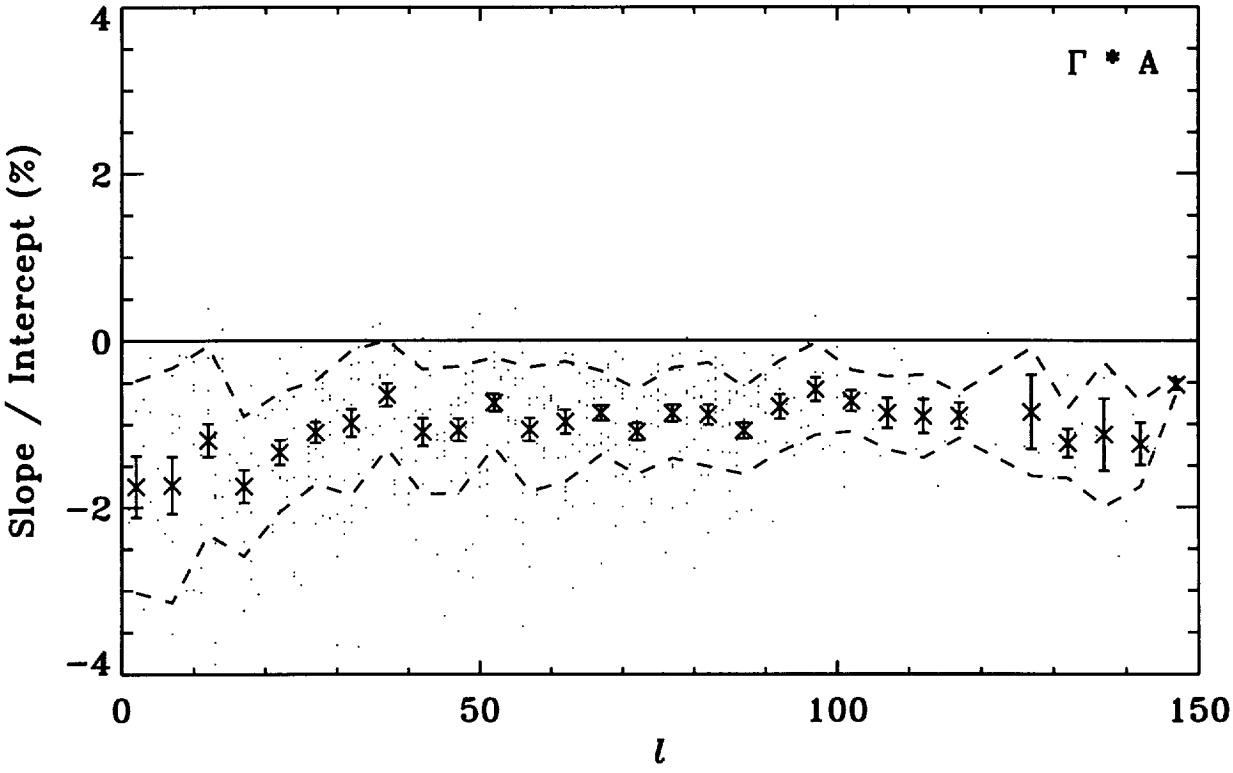
Γ * A
Slope / Intercept (%)
4
2
0
−2
−4
0
50
100
150
l

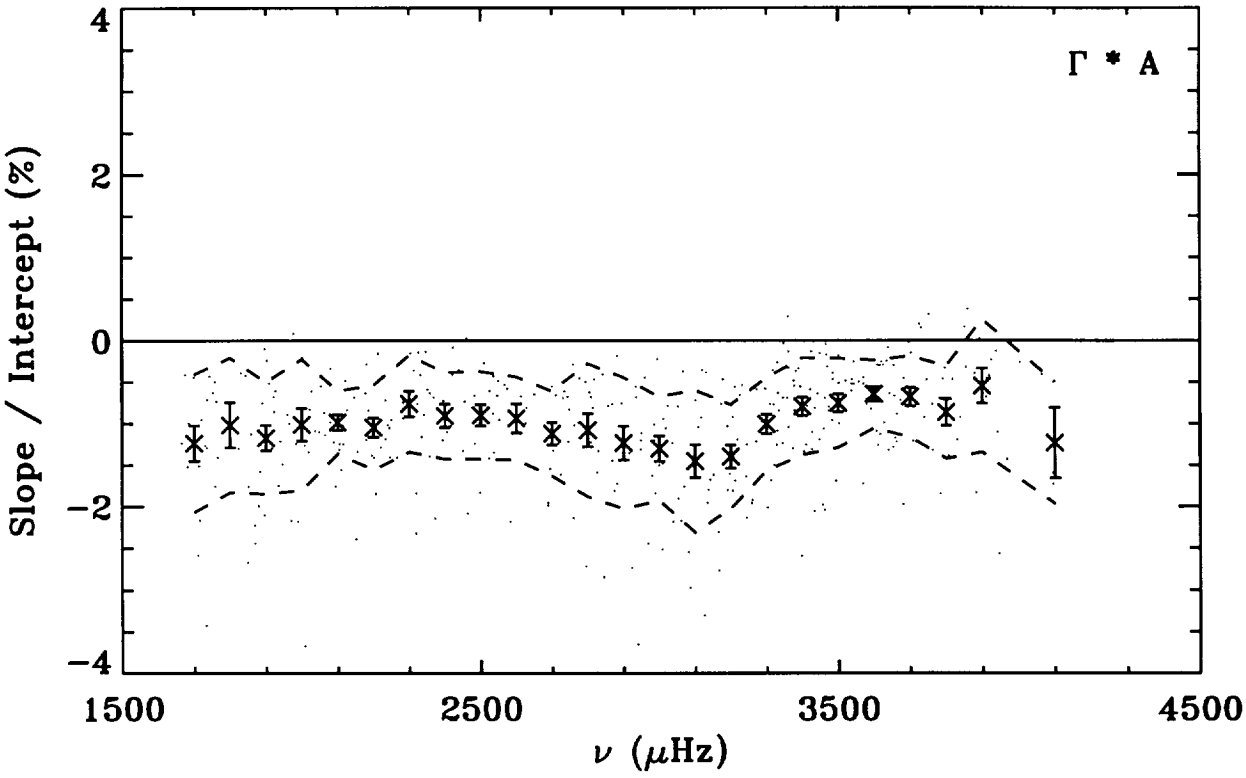
Γ * A
Slope / Intercept (%)
4
2
0
−2
−4
1500
2500
3500
4500
ν (μHz)

Fig. 12

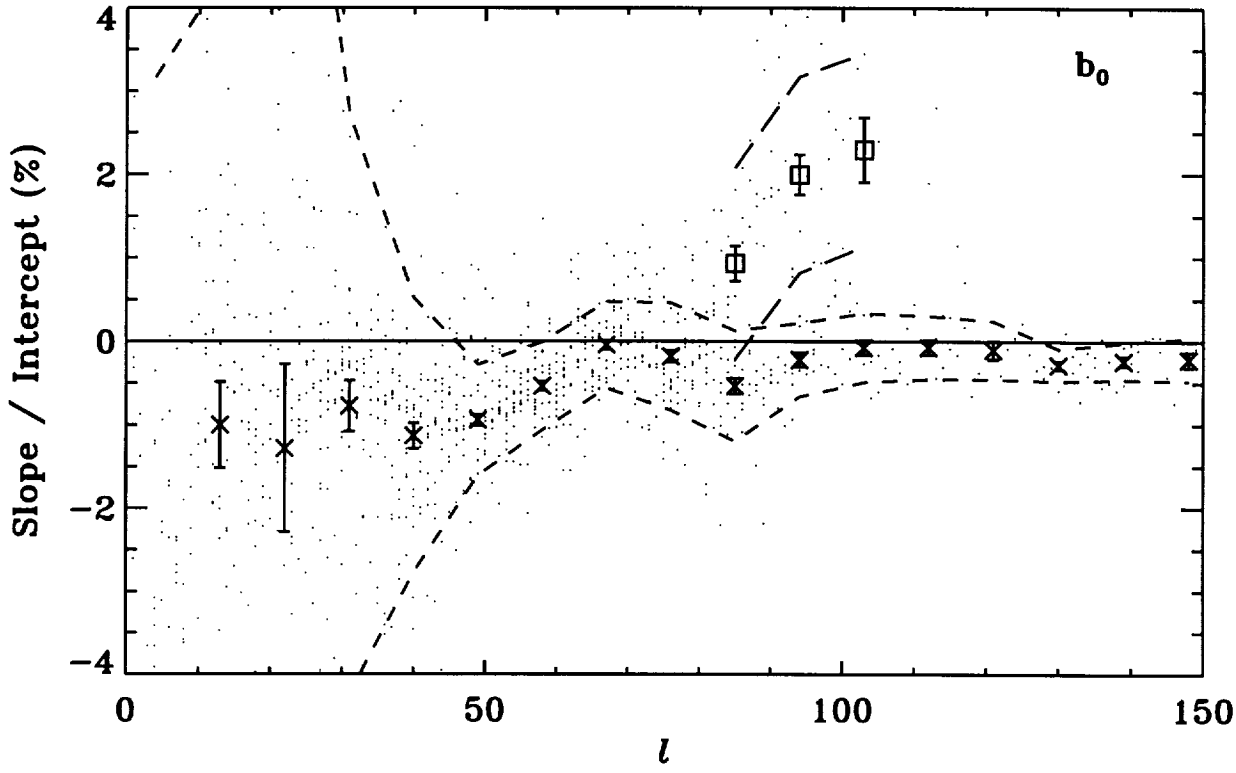
b0
Slope / Intercept (%)
4
2
0
−2
−4
0
50
100
150
l

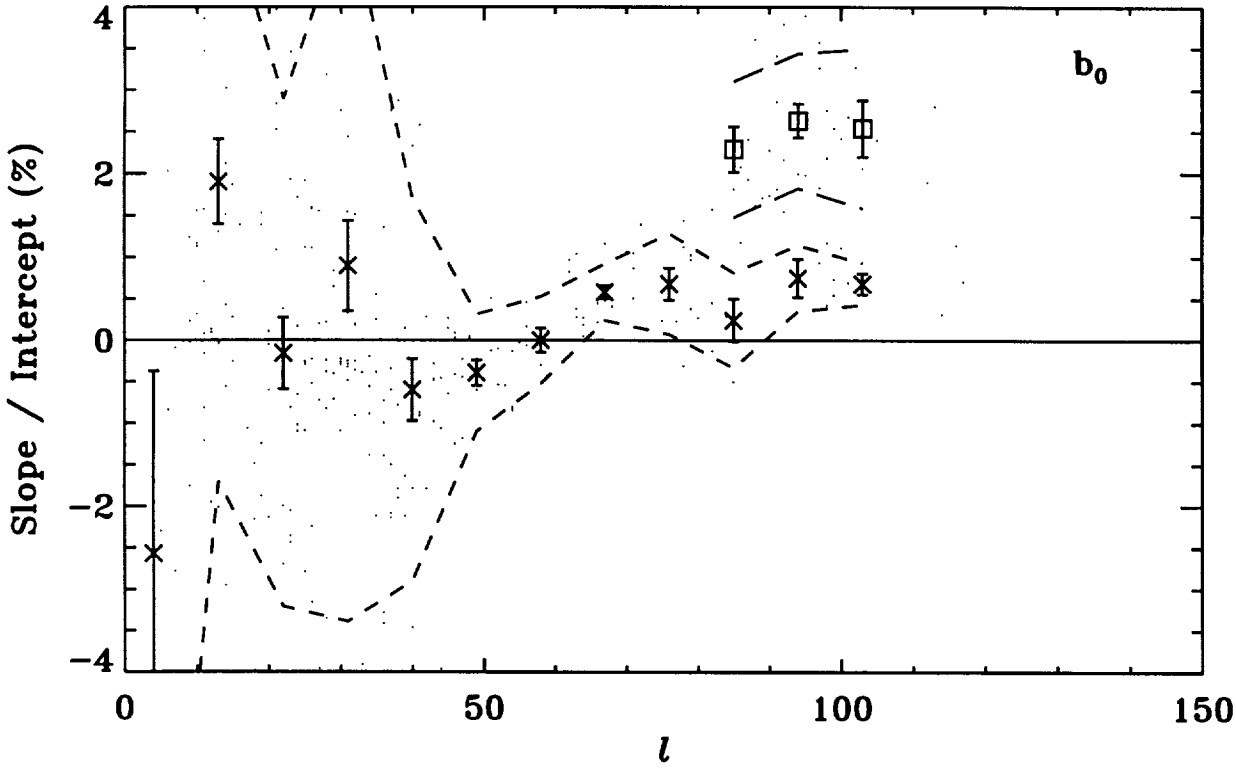
b0
Slope / Intercept (%)
4
2
0
−2
−4
0
50
100
150
l

Fig. 13

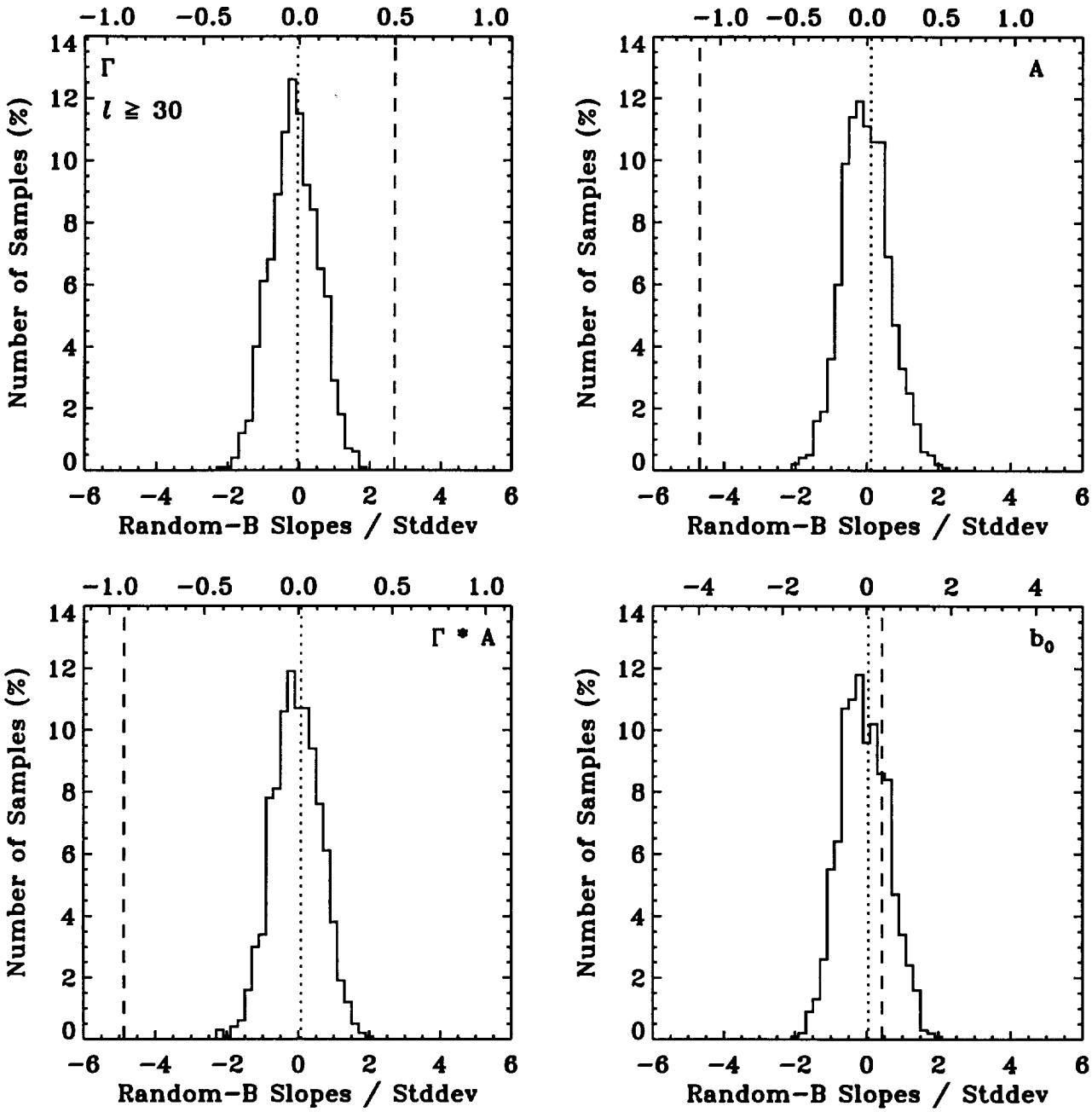

Fig. 14

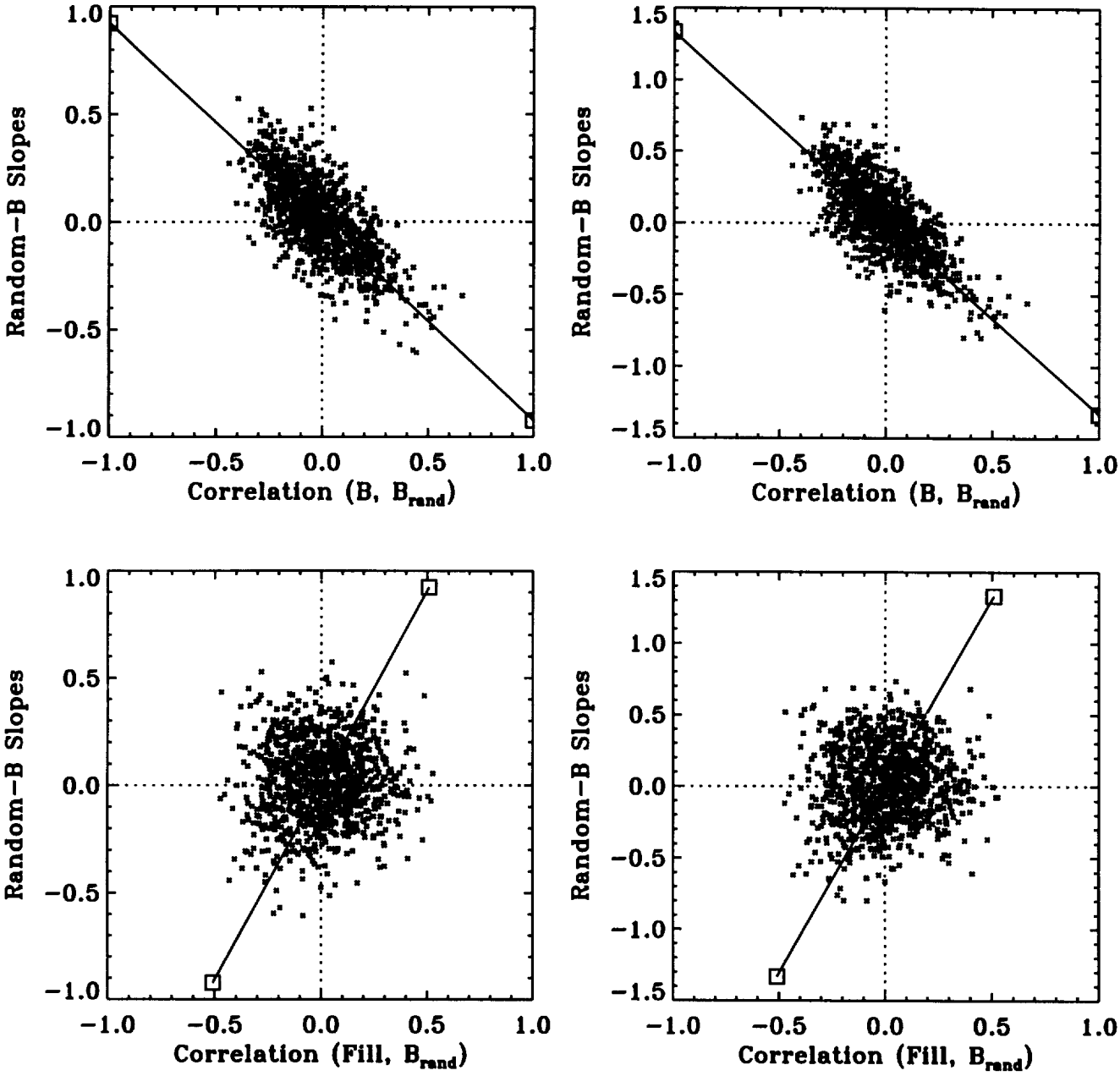
Random−B Slopes
Correlation (B, B$_{rand}$)
Correlation (Fill, B$_{rand}$)
1.0
0.5
0.0
−0.5
−1.0
1.5
−1.5

Fig. 15

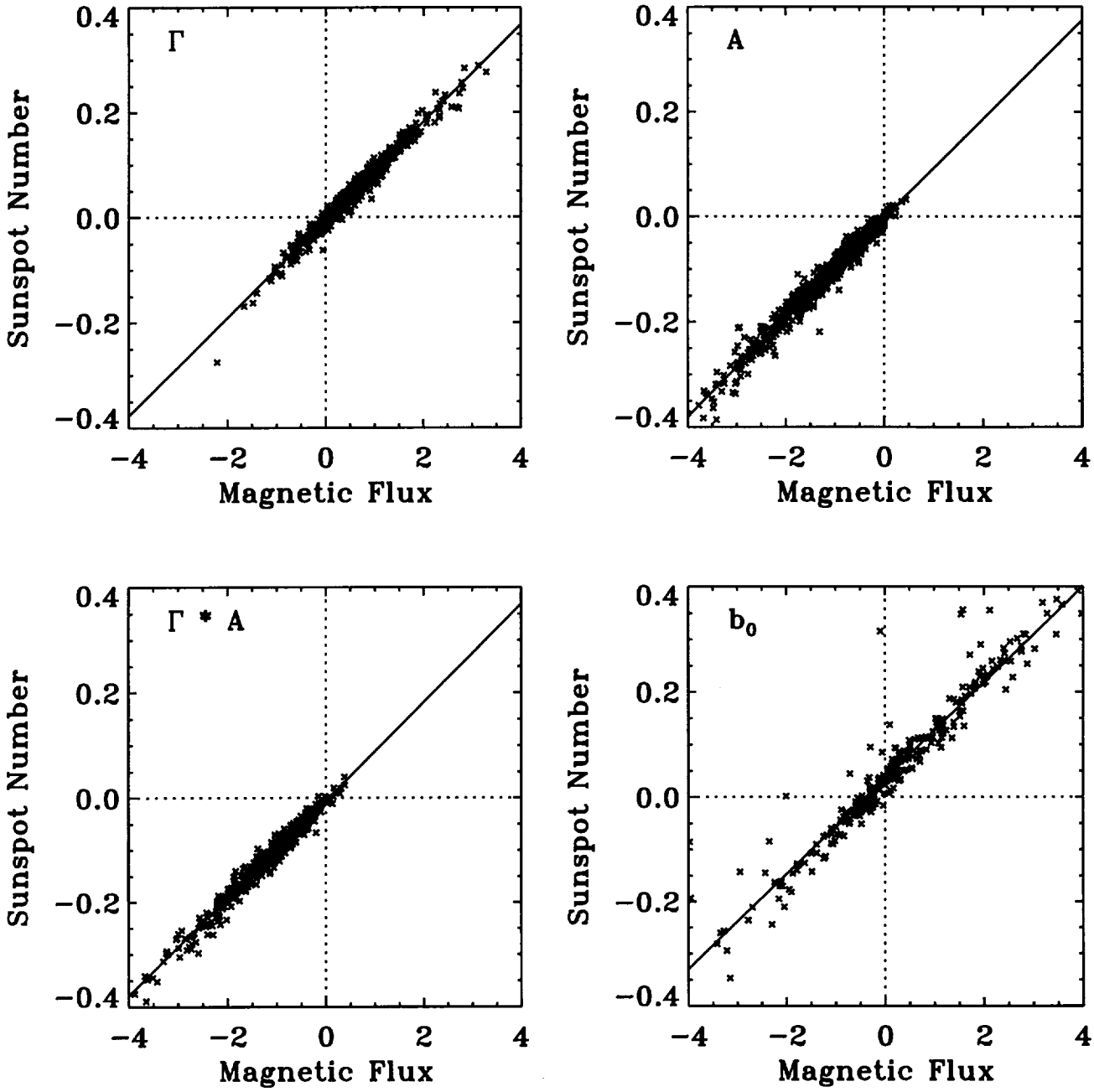

Fig. 16